http://eprints.gla.ac.uk/226985/

Deposited on 8 December 2020

Enlighten – Research publications by members of the University of Glasgow
http://eprints.gla.ac.uk

Deep Draw Induced Wrinkling of Engineering Fabrics

Harrison, Philip[1]* and Gonzalez Camacho, Luis[1]

[1] James Watt School of Engineering, University Avenue, University of Glasgow, G12 8QQ, Scotland

*corresponding author

ABSTRACT

Deep-draw experiments are performed on both glass and carbon fabric both to better understand the origin of wrinkle growth during complex forming experiments and to assess the accuracy, robustness and computational cost of forming simulations of engineering fabrics. During experiments, the shape of the deformed blanks is digitised using two different non-contact measurement techniques (Structured Light Scanning and Photogrammetry). The resulting digital point clouds permit detailed analysis of wrinkle growth and shows that the simulations perform well in predicting the very different forming behaviours of the two fabrics. The sensitivity of wrinkle formation to initial conditions is demonstrated in both experiments and simulations and the direction of wrinkle growth during the forming process is shown to influence wrinkle draw-in; an observation that could potentially be used to mitigate wrinkle draw-in during actual forming processes.

Keywords: wrinkling, engineering fabrics, forming

1 INTRODUCTION

A route to manufacturing advanced composite components of complex geometry is to form a blank, often consisting of multiple sheets of biaxial engineering fabric, into the required preform shape, prior to liquid moulding (Gereke et al., 2013; Pickett, 2018). The 'formability' of

a given part typically depends on the geometry of the component, the inherent or modified (Turk et al., 2020) forming behaviour of the blank and the processing conditions (e.g. blank-holder pressure and pressure/tension distribution (Breuer et al., 1996; Chen et al., 2015; Lin et al., 2007; Nosrat Nezami et al., 2017, 2016). The growing importance of advanced composite materials in the design and manufacture of light-weight products has motivated the drive to develop computer aided engineering tools that can simulate their forming processes (Bussetta and Correia, 2018; Gereke et al., 2013). The goals are usually to predict fibre directions after forming to inform subsequent liquid moulding processes (Vernet et al., 2014) and structural simulations and also to predict possible forming-induced defects, such as wrinkling (Boisse et al., 2011; Harrison et al., 2018b; Hosseini et al., 2017, 2018; Rashidi and Milani, 2018), yarn slippage (Iwata et al., 2019; Labanieh et al., 2018) or decohesion of the fabric (Gatouillat et al., 2013) that can result in reduced quality (or scrap) parts.

Ideally the forming simulations should be fast, accurate, robust, and easy to use. Further, the constitutive model input parameters should be easily measurable via experimental tests (Cao et al., 2008) or else predictable from meso-scale simulations (Creech and Pickett, 2006; Iwata et al., 2019; Wang et al., 2020). In practice, the objectives of speed and accuracy often tend to conflict and the more accurate the simulation, the greater the effort required to determine the relevant material properties. These factors lead to a trade-off, with the optimum simulation approach depending on the user's needs. Kinematic (Hancock and Potter, 2006) and finite-element based approaches (Bussetta and Correia, 2018; Gereke et al., 2013) have been developed and both are commercially available. Kinematic codes lay at one extreme of the accuracy versus speed trade-off; they are fast, producing results in seconds, easy to use and require very little material input data, but they do ignore many aspects of the mechanics involved in the forming process and are therefore limited in terms of both accuracy and their capacity to predict defects (e.g. no wrinkle or yarn slippage predictions) making them less reliable when analysing parts of even modest geometry complexity (Vanclooster et al., 2009). The no-slip boundary condition typically used in kinematic codes also makes them better adapted to predicting the behaviour of 'sticky' prepregs that adhere to the tooling and less appropriate for engineering fabrics that tend to slide across the tooling during processing

(Hancock and Potter, 2006). Various finite element-based methods have been proposed and their speed, accuracy and predictive capability vary greatly depending on: the modelling approach (e.g. the use of bespoke finite element formulations or the combination of multiple different structural finite elements), the accuracy of the constitutive model and associated material input data (e.g. which stiffnesses can be neglected, or which non-linearities can be ignored), the accuracy of friction/adhesion behaviour (Mulvihill et al., 2017; Najjar et al., 2014; Nosrat Nezami et al., 2016) and the numerical solution method (e.g. implicit versus explicit) (Pickett, 2018).

Unlike continuum materials, the fibrous nature and meso-structure of engineering fabrics means that they have several non-linear stiffnesses, including: (i) **tensile stiffness** along the fibre directions (Boisse et al., 2001; Potluri and Thammandra, 2007), (ii) **shear stiffness** associated with rotation of the two fibre directions (Aimene et al., 2010; Cao et al., 2008; Harrison et al., 2012, 2008; Hosseini et al., 2018, 2017), (iii) **out-of-plane bending stiffness** in each of the two fibre directions (Cooper, 1960; de Bilbao et al., 2010; Harrison and Hartel, 2016; Hu, 2004; ISO, 1998; Lammens et al., 2014; Lomov et al., 2003; Peirce, 1930; Plaut, 2020, 2015), (iv) **in-plane bending stiffness** in each of the two fibre directions (D'Agostino et al., 2015; De Angelo et al., 2019; Dell'Isola and Steigmann, 2014; Ferretti et al., 2014; Giorgio, 2016; Giorgio et al., 2016, 2018; Harrison, 2016; Harrison et al., 2018a; Scerrato et al., 2016; Steigmann and Dell'Isola, 2015; Turco et al., 2016), (v) **torsional stiffness** in each of the two fibre directions (Cooper, 1960; D'Agostino et al., 2015; De Angelo et al., 2019; Giorgio, 2016; Giorgio et al., 2016; Harrison et al., 2018a; Lomov and Verpoest, 2006; Steigmann and Dell'Isola, 2015) and (vi) **through thickness compressive stiffness** (Chen and Ye, 2006; Pazmino et al., 2014; Wang et al., 2020). To complicate matters further some of these stiffnesses are coupled (Abdiwi et al., 2013, 2012; Boisse et al., 2001; Komeili and Milani, 2016; Nosrat-Nezami et al., 2014). A challenge is to accurately include most, if not all, of these stiffnesses and their associated couplings within the simulation while minimising computational and materials characterisation costs. The goal of reducing reliance on experimentation to determine material input data has also motivated the development of meso to macro modelling approaches (Creech and Pickett, 2006; Iwata et al., 2019; Wang et al., 2020); an approach that is becoming

increasingly viable due to the falling cost of computation and improvements in meso-macro simulation methods (Wang et al., 2020).

The FE-based comprehensive modelling approach used in this investigation was initially described in (Harrison, 2016) and further expanded to include an independent torsional stiffness in (Harrison et al., 2018a). The finite element mesh uses a combination of membrane and beam elements, connected using zero torque 'hinge' connector elements in a 'mutually-constrained pantographic beam and membrane mesh' (see Section 3 for further description). Homogenisation theory permits decoupling and independent control of the various fabric stiffnesses listed above (in the current model, through-thickness compressive stiffness is ignored). The ability of the modelling approach to accurately predict the specimen size dependent shear kinematics and wrinkling onset angle in a uniaxial bias extension test was demonstrated in (Harrison et al., 2018a) and the model's equivalence with a generalised second order gradient continuum approach to modelling engineering fabrics was shown in (Giorgio et al., 2018). The experimental method of determining the shear, bending and torsional stiffnesses required by the model was demonstrated using two simple, well-established tests: the cantilever bending test (de Bilbao et al., 2010, 2008; Harrison, 2016; Hu, 2004; Peirce, 1930; Plaut, 2020, 2015; Yu et al., 2020) and a modified version of the uniaxial bias extension test (Cao et al., 2008; Giorgio et al., 2018; Harrison et al., 2018a). The latter have been used to characterise the forming mechanics of two different engineering fabrics, a plain weave glass fabric and a 2x2 twill weave carbon fabric (Harrison et al., 2018b) (see Section 2.1 for further details). The glass fabric is notably stiffer than the carbon fabric. The objectives of the current work are:

- to demonstrate an experimental setup that can be used to accurately characterise the wrinkling behaviour of engineering fabrics during a deep draw forming process,
- to evaluate the accuracy, computational cost and robustness of the modelling approach in a complex forming scenario. The focus is on evaluating the model's ability to predict fabric wrinkling,

- to better understand wrinkle development during forming of engineering fabrics, to explore the possibility of controlling the direction of growth of wrinkles and to understand the effect this has on wrinkle draw-in,
- to evaluate the use of the two experimental scanning techniques for the purpose of wrinkle characterisation.

The structure of the remainder of the paper is as follows: in Section 2 experimental aspects of the investigation are described including a description of the fabrics, the experimental setup and measurement techniques, in Section 3 the numerical modelling approach is described, Section 4 presents and discusses the results of the investigation. Conclusions are given in Section 5.

2   FORMING EXPERIMENTS

Deep draw tests were conducted using a cylindrical punch to push an initially flat circular fabric blank, down into a circular die containing a central hole, shown and described in detail Section 2.2. In so doing the fabric inevitably starts to shear and eventually wrinkles, with the wrinkling becoming more pronounced, at least during the initial phase of the test, as the blank is pushed further down into the hole. The setup therefore provides a controlled method to characterise the mechanics of wrinkling of sheared fabrics. The experimental set-up is designed to allow unrestricted growth of wrinkles in the region between the blank-holder and die. A detailed description of the forming set-up is provided in Section 2.1. To explore the influence of material properties, tests were conducted using two different types of engineering fabric (see Section 2.2) and in each case experiments were performed both with and without an upper blank holder.

2.1   MATERIALS

The same two woven engineering fabrics as those characterised in (Harrison et al., 2018b) have been used: **Fabric 1** is a plain weave glass fabric (from Allscot - ECK 10) with an areal density of 0.30 ± 0.01 kgm^{-2} and an average thickness of 0.26 ± 0.02 mm (see Fig 1a). **Fabric 2** (see Fig. 1b) is a 2×2 twill weave engineering carbon fabric woven from Mitsubishi Pyrofil TR30S 3K tows

(distributed by EasyComposites) with an areal density of 0.21 ± 0.002 kgm^{-2} and an average thickness of 0.2 ± 0.02mm (see Fig 1b). No binder is applied to either of the fabrics. Despite the more open structure of the glass fabric (compare Fig 1a and 1b), manual handling indicates the glass fabric is significantly stiffer than the carbon fabric, a point confirmed by characterisation tests (Harrison et al., 2018b). Mechanical forming properties used in the numerical simulations are provided in Appendix A. All forming experiments were conducted using just a single sheet of woven fabric.
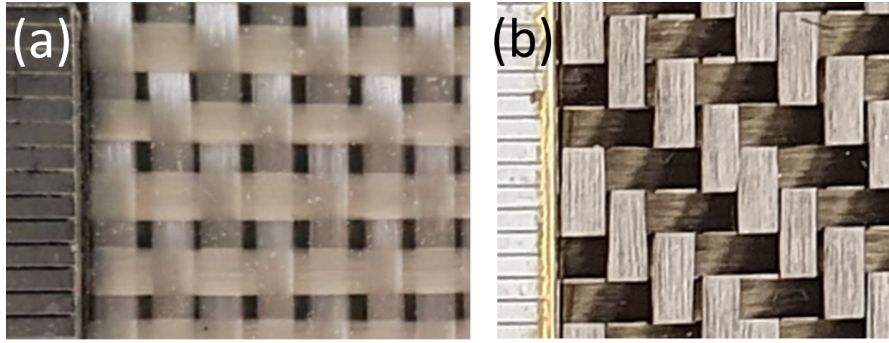

*Figure 1. (a) **Fabric 1**; a plain weave glass fabric and (b) **Fabric 2**; a 2×2 twill carbon fabric. Ruler increments = 1 mm.*

2.2 EXPERIMENTAL FORMING SET-UP

The experimental setup is shown in Figure 2. It consisted of a Perspex turntable made of two components; (a) a stationary square **lower base** fixed to the test bed of a Zwick universal test machine and (b) a circular **upper base** measuring 460mm in diameter. The square lower base contained a circular recess (3mm deep) into which the upper base slotted. The upper base was able to rotate within the confines of the recess; a requirement for recording Structured Light Scanning data from different angles (see Section 2.4.1). Markings (c) were added to the lower and upper base plates to indicate 45° rotation-mark increments, facilitating 3-d scanning of the formed fabric. (see Section 2.4.1) A vertically orientated **linear bearing** (d) was fixed to the upper base along with four **wooden columns** (e)**,** each of 105 mm height. A **lower blank holder** (f), in the shape of a circular Perspex ring was attached to the top of the columns. An **upper blank holder**, weighing 786g, was attached to the linear bearing and supported from below by the lower blank-holder. The upper blank-holder was thus able to move freely in the vertical, *z*,

direction but constrained in the horizontal *x-y* plane. The upper blank holder consisted of a lower Perspex ring (g_1) bonded to an annular Perspex plate (g_2). Only the lower ring of the upper blank holder contacted the blank. The upper plate provided a means of adding extra weight to the upper blank holder, though in this investigation only the self-weight of the blank holder was considered. Both the **female die** (h) and **male punch** (i) were 3-d printed from ABS. The dimensions of the various parts used in the setup (see Figure 3) are: *Punch diameter = 50 mm with 4.5 mm fillet radius around the edge of its flat bottom surface. Die inner hole diameter = 60mm. Die outer diameter = 120mm. Die fillet radius = 15mm. Inner diameter of blank-holders =260 mm, outer diameter of blank-holders = 320mm. Fillet radius on edges of blank-holders = 3mm.*

Without further processing, the 3-D printing produced a very rough striated surface finish. The latter results in a very high friction coefficient between the tooling and the fabric specimens (see Section 2.3), consequently, the surface finish of the die was smoothed using silicon carbide sandpaper (CW-240 grade) and acetone. The upper surface of the die was positioned at the same height as the upper surface of the lower blank-holder. The test specimen, a circular fabric blank of ~480mm diameter, was cut using a simple bespoke cutting tool (a rotating knife mounted on a rotating arm), designed to minimise unintentional pre-shearing of the blank during cutting. Mitigating pre-shear is important in creating repeatable results, a point emphasised in (Alsayednoor et al., 2017). To aid in locating the blank centrally in the forming setup, a 'Sharpie' gold marker pen was used to mark the centre of the fabric blank. Talcum powder was used to reduce reflectivity of the upper surface of the blank, a step that also influenced the tool-fabric friction (see Section 2.3). The open nature of the experimental set up is designed to allow uninhibited growth of wrinkles in the annular region between the die and blank holder, without the friction and kinematic constraint associated with a continuous lower blank holder plate.
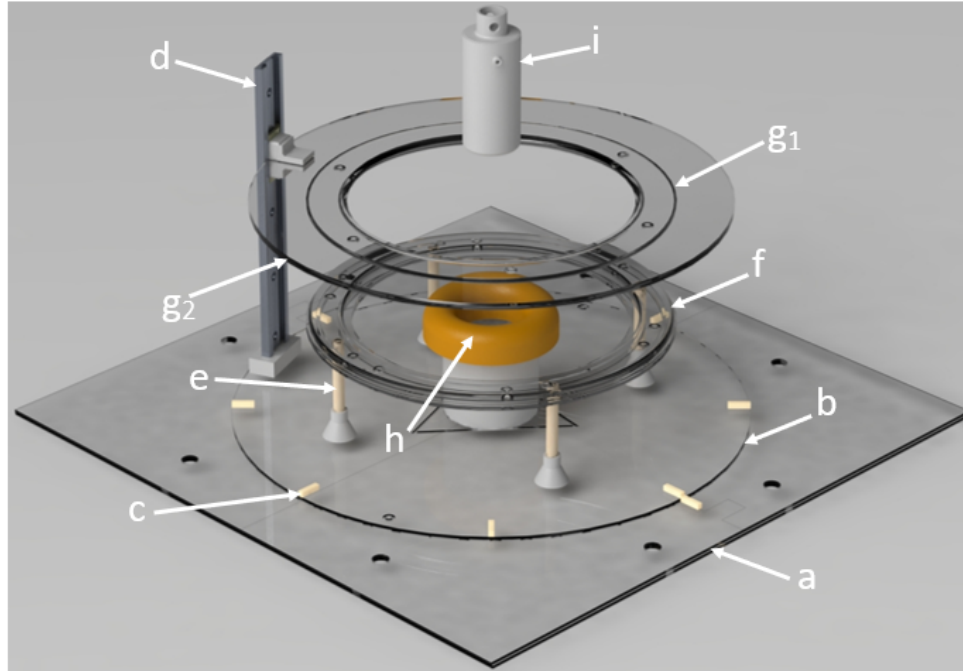
Figure 2. CAD representation of forming set up consisting of: (a) Perspex lower base, (b) Perspex upper base, (c), 45° rotation-mark increments, (d) linear steel bearing, (e) wooden support columns, (f) Perspex lower blank-holder, (g$_1$) Perspex bottom ring of upper blank-holder, (g$_2$) Perspex top annular plate of upper blank-holder, (h) 3-D printed female die and (i) 3-D printed male punch.
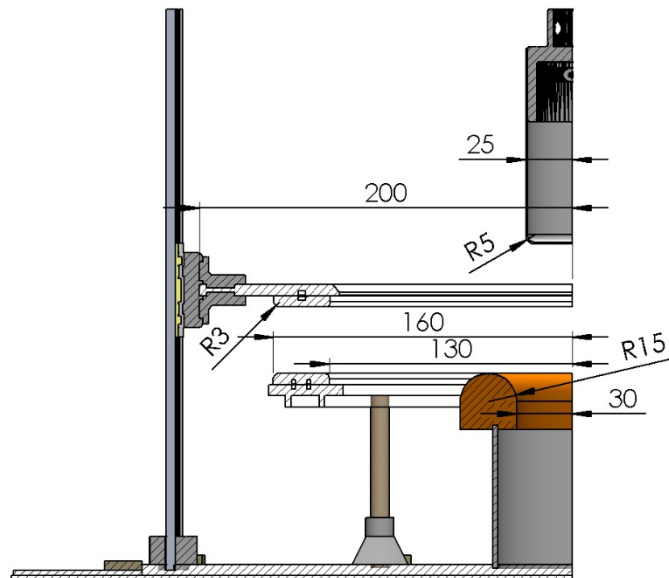

Figure 3. Cross-section through centre of the axisymmetric arrangement of tools (apart from the stand which sits to one side of the set-up, as shown in Figure 2), showing the male and female tools, the blank-holder arrangement and the blank-holder supporting stand (dimensions in mm).

2.3 TOOL-FABRIC FRICTION

A simple sloping board arrangement was used to measure friction between carbon fabric and the Perspex blank-holder (Costantini et al., 2020; Mercier, 1930). The carbon fabric covered the board and the blank holder was placed on the fabric. The board was tilted until the blank holder began to slip. An iPhone inclinometer app was used to measure the inclination angle. A digital camera (Casio EX-ZR700) was used to record the test to better identify the onset of slip. The test was repeated 10 times before calculating the average and standard deviation in the inclination angle, α, at the onset of slip. The Coulomb model was used to calculate the static friction via, $\mu s = tan\alpha$. The effect of treating the carbon fabric with talc was also investigated. A normal pressure of just ~0.0007 Bar was generated by the self-weight of the blank holder. Under this condition, the coefficient of static friction between the Perspex and glass fabric was measured to be 0.30+/-0.02 for the untreated glass fabric and 0.26+/-0.008 when treated with talc. Similar measurements were made for the carbon fabric as 0.33+/-0.02 for the untreated carbon fabric and 0.26+/-0.006 when treated with talc, here the error is given by the 95% confidence interval. Similar values to that found for the untreated carbon fabric are noted in the literature, though values tend to increase with increasing amounts of sizing or binder and decrease with increasing applied normal pressure, making direct comparison with other published results difficult (Mulvihill et al., 2017; Najjar et al., 2014; Nosrat Nezami et al., 2016). For simplicity and because only the upper surface of the blank was treated with talc, a coefficient of friction of 0.30 was used for all fabric/tool interactions in the simulations.

2.4 POSITION MEASUREMENT TECHNIQUES

Two types of 3-D image acquisition techniques were used to record the shape of the surface of the formed fabric after testing: (a) Structured Light Scanning (SLS) (Yu et al., 2020) and (b) photogrammetry. By appropriate digital processing (see Section 2.6), direct quantitative comparison between experiment and numerical simulation can be conducted. One aim of this investigation is to evaluate the relative utility of these two measurement techniques in quantifying wrinkling behaviour (see Section 4.2).

2.4.1 Structured Light Scanning (DAVID SLS-3 Structured Light Scanner)

A DAVID SLS-3 Structured Light Scanner (now marketed as a HP 3-D Scan system) was used. Structured light scanning uses the distortion of a projected light pattern when cast on a 3-D object, to reconstruct a 3-D image of the object's surface shape (see Figure 4). (The grid lines marked on the sheet visible in Figure 4 are not required in this investigation but can be used to measure shear angles). The object must have an opaque surface and reflections from the surface should be avoided as these affect the ability of the camera to capture the projected light pattern, resulting in a low-quality scan. Captured images are processed by dedicated software through time and spatial modulation. Correct calibration of the SLS system is key to obtaining accurate results. Once calibrated the SLS system must remain stationary, turn-tables are therefore typically used to generate 360° images of 3-D objects. The 3D data gathered from the scanning process is represented as a point cloud mesh. The quality of the results can be improved by taking multiple overlapping scans of the target object. Projector settings used in the experiments were: mode F, auto keystone = off, manual keystone = 0 and camera settings used were: exposure 1/60s, camera angle ~21°, distance on rail ~280mm.
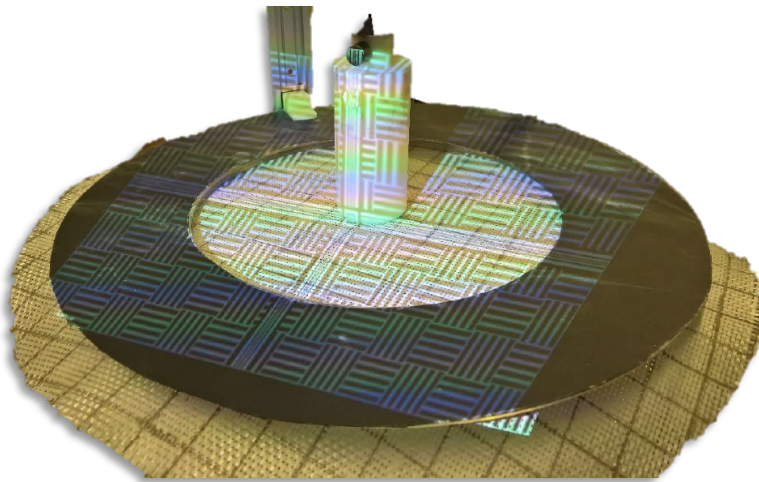

Figure 4. (a) Example of structured light pattern projected by SLS system onto glass fabric prior to starting the test. In this experiment the region of interest for the scan is the area between the punch and the upper blank-holder, the Perspex blank-holder has been covered with black card to reduce reflections.

2.4.2   Photogrammetry (3DF Zephyr)

The photogrammetry software used in this investigation was 3DF Zephyr. The technique uses the features of the scanned object to reconstruct a 3-D image and requires a digital camera (here a Casio Exilim EX-ZR100) to take a minimum of 50 photographs of the specimen from different perspectives. The digital images are then uploaded into the software for reconstruction of the 3-D image.

2.5   EXPERIMENTAL FORMING METHOD

Prior to each experiment the talc-treated blank was positioned centrally on top of the die and lower blank holder, ready for the forming experiment to begin. During forming tests, the blank was drawn into the die by the downward motion of the punch. The punch force and digital videos were monitored during the tests. At the end of the test, the punch was stopped, and the form of the deformed blank was measured using the position measurement techniques described in Section 2.4

2.5.1   Experimental Method 1: Stochastic Wrinkling

Typically, one dominant wrinkle occurred in each quadrant of the blank during forming, though these dominant wrinkles were found to grow both upwards (bulges) and downwards (depressions). To understand the nature of wrinkle growth direction, 10 experiments were conducted without the upper blank holder: 5 with glass and 5 with carbon fabric and the number of bulges and depressions in each experiment were counted. A punch travel of 50 mm was used for all these initial tests. For the glass fabric, depressions were found to occur in ~15 % of the quadrants, whereas for the carbon fabric depressions were found to occur in ~42.5% of the quadrants. The reason for the random nature of wrinkle growth direction is most likely due to the occurrence of random perturbations. These arise due to the process of cutting, moving and placing the blank in the experimental setup and is also due to the fabric's propensity to sag due to self-weight loading. Because the carbon fabric is much more compliant than the glass fabric, it is more susceptible to perturbations. Once a wrinkle begins to form it continues to grow in the same direction, at least until the later stages of the test where changes in direction are possible. Small initial perturbations are enough to determine the direction of growth.

2.5.2 Experimental Method 2: Controlling Wrinkle Direction

The random growth behaviour is not seen in the simulations of this investigation (see Section 3), where unless an intentional initial perturbation is applied, the dominant wrinkle in each quadrant of the blank is always predicted to grow upwards. In order to generate experimental results suitable for direct comparison with numerical predictions, the sensitivity of wrinkles to initial perturbations was used to control the direction of wrinkle growth; wrinkles growing in a given direction could be reversed by lightly pushing the fabric (by hand), in the desired direction during the initial stages of the test. **In the first series of tests, four upward bulges were created in each experiment**, while **in the second series of tests four downward depressions were created in each experiment**. The location of the 'seeding' was important in ensuring the bulge or depression continued to grow autonomously. The seeding was most effective when positioned at smaller radial distances away from the centre of the setup (about 10-20 mm beyond the rim of the die). The manual approach meant that the perturbation amplitude was somewhat variable, but usually in the range of 2 to 3 mm. During practical manufacture of actual parts, out-of-plane wrinkles are usually only problematic if they are drawn into the useable region of the manufactured part, i.e. if consolidated between the male and female tools (Turk et al., 2020). Wrinkles occurring outside this area are usually simply cut away and discarded. If the blank is unconstrained in the vertical direction during the forming process, for example for advanced thermoplastic composites that sometimes use a frame plus springs to induce tension in the forming blank (Chen et al., 2015; Harrison et al., 2013), rather than using a upper and lower blank holder (Lin et al., 2007; Nosrat Nezami et al., 2017), wrinkles can form either upwards (bulges) or downwards (depressions). The motivation behind creating wrinkles in the two directions in these experiments was partly to determine whether wrinkle direction has any influence on the propensity towards wrinkle draw-in, down into the die, and partly to evaluate the predictive capacity of the simulations under the two scenarios (bulges vs depressions).

In each test series, four different forming cases were examined to provide a range of forming conditions, **Case 1:** glass fabric without upper blank holder (Figures 5a and 6a) **Case 2:** glass fabric with upper blank holder (Figures 5b and 6b), **Case 3:** carbon fabric without upper blank

holder (Figures 5c and 6c) and **Case 4:** carbon fabric with upper blank holder (Figures 5d and 6d). For the first series (bulges), all tests were repeated three times to investigate the repeatability of the experiments (see Section 4.1). A preliminary qualitative full-field comparison between experiments and simulations is provided in Figures 5 and 6 for the two series of tests.
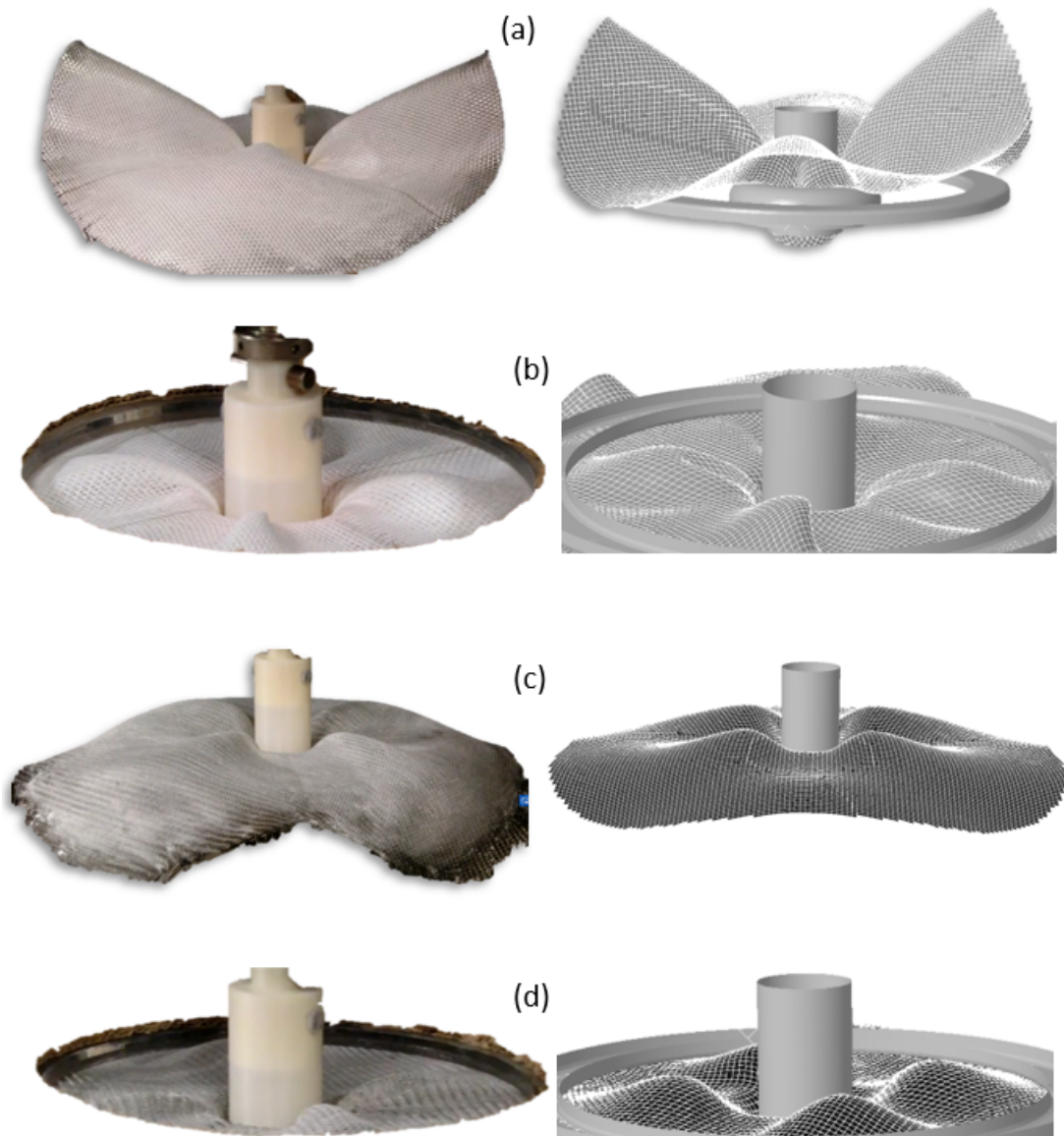

Figure 5. *Various matched isometric views of experiments and simulations for **upward growing wrinkles**: (a) glass fabric without blank-holder, punch depth=50mm, (b) glass fabric with blank-holder, punch*

depth=50mm, (c) carbon fabric without blank-holder, punch depth=40mm, (d) (b) carbon fabric with blank-holder, punch depth=40mm. Beam elements show tow directions.
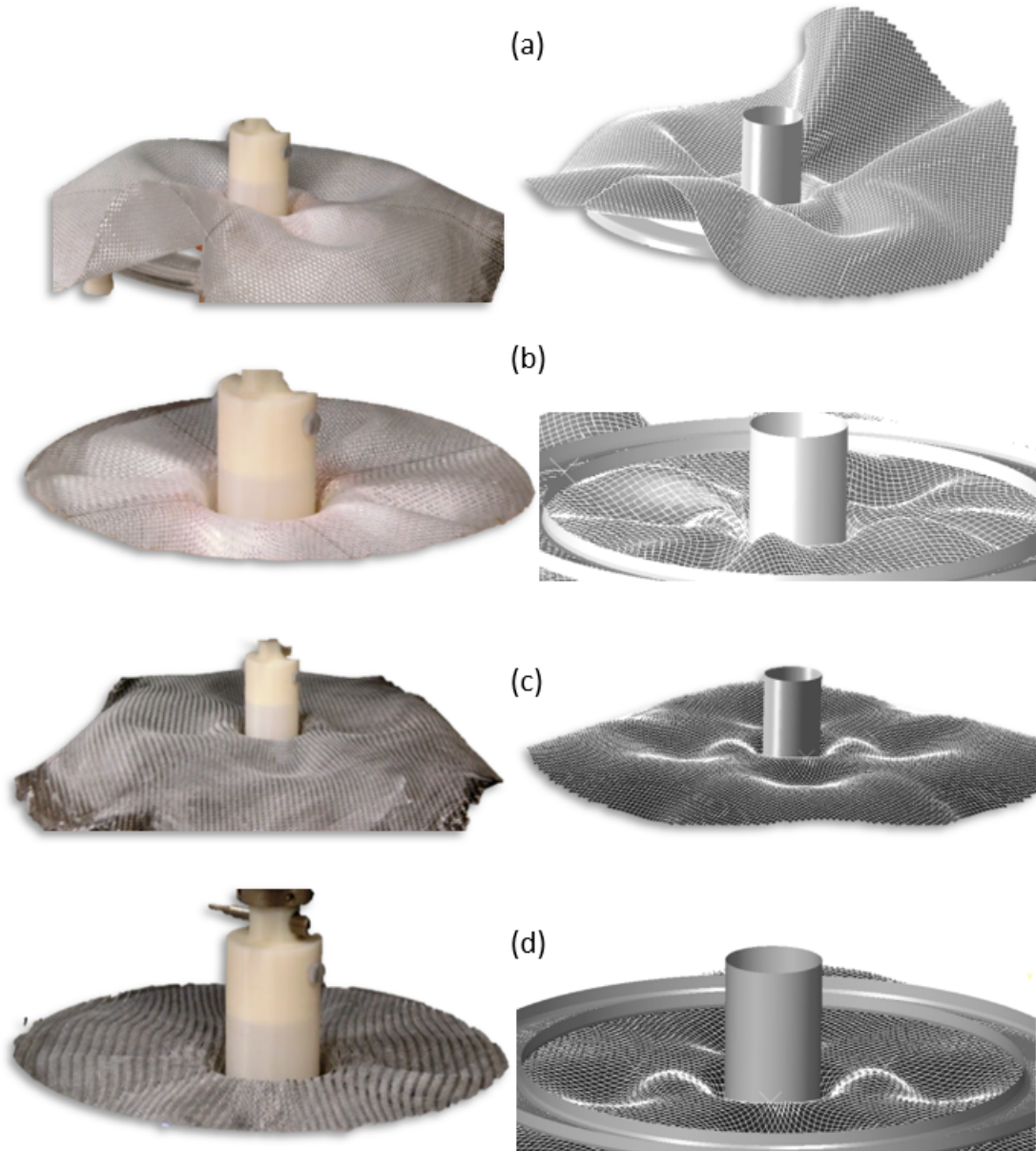

*Figure 6. Various matched isometric views of experiments and simulations for **downward growing wrinkles**: (a) glass fabric without blank-holder, punch depth=40mm, (b) glass fabric with blank-holder, punch depth=60mm, (c) carbon fabric without blank-holder, punch depth=40mm, (d) carbon fabric with blank-holder, punch depth=40mm. Beam elements show tow directions.*

The simulations capture the generic behaviour observed in the experiments; the dominant wrinkles are always orientated along the bias direction of the fabric, this is perhaps more easily

visible in Figure 5 than in Figure 6, though the troughs of the depressions were found to occur around same polar positions as the peaks of the bulges. Further, the glass plain weave fabric has a greater tendency towards wrinkling than the twill weave carbon fabric, i.e. the glass fabric is less formable than the carbon fabric. There are notable differences between the simulations and experiments, for example, the gravitational sagging tends to be less in the simulations. Potential reasons for differences between experiments and simulations are discussed in Section 5. More detailed scrutiny of results using the digital data provided by the image capture technology is provided in Section 3. The final **punch travel depths** used for the detailed comparison (see Section 3.1) in the first series of tests (upward bulges) were initially chosen based on limitations imposed by the numerical simulations which failed at different punch depths, depending on the specific experiment. For the first series of tests on carbon fabric, the draw depth was set to 40mm at a rate of 20mm/min. For the glass fabric, the draw depth was set to 50mm at a rate of 25 mm/min. Later in the investigation, the robustness of the numerical simulations was improved by changing various numerical parameters (e.g. the mesh hinge length and the Rayleigh damping values), allowing them to reach deeper punch travel depths. However, it was noted that in both the experiments and the simulations, the form of the wrinkles became less regular and repeatable as the depth of draw increased and were therefore less conducive for comparison purposes. **Punch travel depth in the second series of tests** (downward depressions) was decided for similar reasons for the two carbon fabric experiments; the draw depth was set to 40mm at a rate of 20mm/min for both tests. Experiments on the glass fabric were stopped at the point that wrinkles appeared to begin to be drawn down into the inner region of the die. Consequently, the experiment involving the glass with no blank holder was stopped at a punch depth of 40mm while the glass with blank holder experiment was stopped at a depth of 60mm.

2.6   DATA PROCESSING

An important aim of the investigation is to compare the results of simulation and experiments as closely as possible. To do this, the scan data (see Section 2.4) is first converted into a common 'point cloud' format using MeshLab ("MeshLab," n.d.); an open source system for processing and editing 3D triangular meshes. Data from the experiments are imported into

MatLab where they are first adjusted to ensure they share the same length scale and orientation as the simulation results. Next a selection of data is extracted from the full data set for comparison purposes. Given the axisymmetric nature of the tooling and blank holder used in the experiments, a convenient comparison can be made by selecting data points lying within the confines of a predefined annular ring, using a polar plot of the angular position versus height of the surface (z-coordinate). In this way the amplitude of the wrinkles in both experiment and simulation can be directly compared in the same graph. The radial position of the annular ring, r, was chosen to correspond to the radial position of the maximum wrinkle height predicted in each simulation. To gather enough data points for a meaningful comparison, the width of the annular ring was chosen to be r +/-2mm, an example is shown by the 'outer ring' of data points highlighted in green in Figure 7.
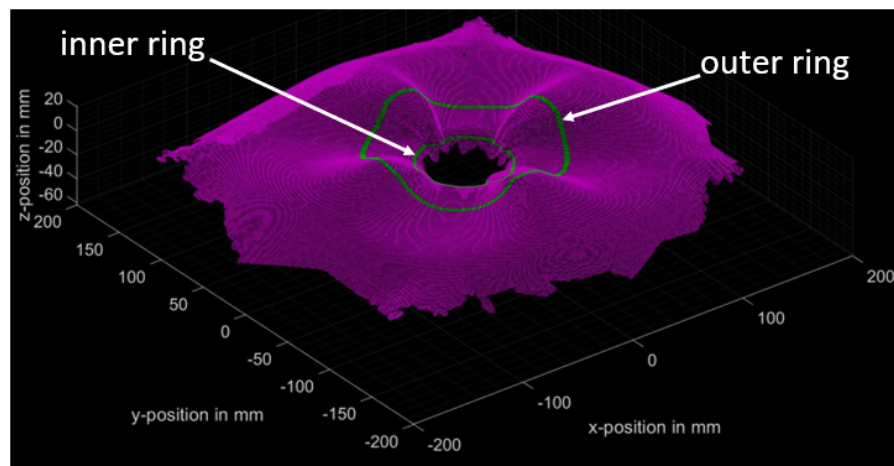

Figure 7. *Point cloud plotted in MatLab, produced by SLS for carbon fabric without blank holder. The green rings indicate data points used for creation of polar plots in Section 4*

During manufacture, wrinkles become problematic if they are drawn in, and then consolidated into the useable region of the manufactured part. It is therefore interesting to measure and predict the size of any wrinkles that are drawn from the flange area of the blank, down into the die hole. To capture these data points, both vertical and radial ranges were used to define a volume near the interior edge of the die, from which data points could be extracted to examine wrinkle draw-in. The top surface of the die was taken to be z=0 mm and the depth range used to extract data was defined between $-5.6 < z < -3.2$ mm. Any data values falling beyond

r=40mm were excluded from the data extraction (see rectangular region in Figure 8). The extracted data was then used to plot the shape of the fabric within this region, as viewed from above (see results in Section 4.3.1).
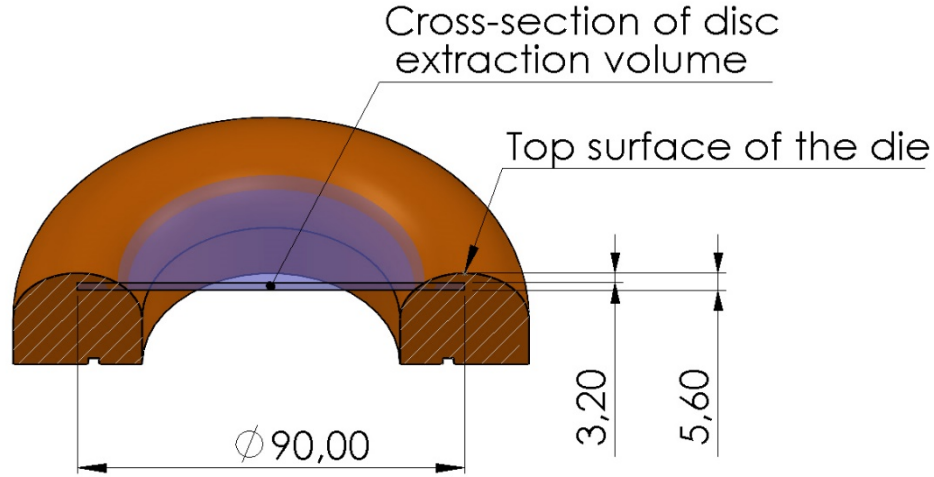

Figure 8. *Cross-section through central die. Rectangle shows the region used to collect data points falling inside a collection volume, creating the green 'inner ring', highlighted in Figure 7.*

3 NUMERICAL SIMULATION METHOD

A semi-discrete modelling approach implemented within a commercial finite element code (Abaqus Explicit[TM]) has been employed to simulate the forming process. This involves the use of a 'mutually constrained pantographic beam and membrane mesh' (Harrison, 2016). Using appropriate homogenisation (Harrison, 2016; Harrison et al., 2018a), linear elastic Timoshenko beam elements (Type B31) are used to model the tensile, bending and torsional stiffnesses of the fabric while the membrane elements (Type M3DR4), implemented with an appropriate constitutive equation (Harrison et al., 2011; Yu et al., 2002, 2005) model both the shear and contact/friction behaviour of the fabric. Zero torque hinge elements are used to connect the beam and membrane elements. A hinge length of just 10^{-8} m was found to give the most robust results. The side length of the initially square membrane elements, and hence the beam element length, were both set at 4mm. Mesh sensitivity studies indicated some degree of mesh dependence between element length and wrinkle development, especially when the radius of

curvature of wrinkles approaches the mesh element length. The current mesh density was found to be the optimum in terms of accuracy and simulation time. Ideally, adaptive meshing would be performed in regions containing high wrinkle curvature, though this capability is not currently available with the proposed modelling approach.

Mechanical forming properties for the two fabrics have been characterised previously and are reported in (Harrison et al., 2018a, 2018b), for convenience they are summarised in the Appendix. A penalty contact condition was applied between the surface of the membrane elements and the rigid body tooling. The coefficient of friction used for all fabric/tool interactions in the simulations was 0.3 (see Section 2.3). The simulations were run without mass scaling, but with velocity scaling (around 300x faster than the experiments) (Pickett, 2018). Numerical investigations have shown that inertial effects introduced by excessive use of mass or velocity scaling tend to suppress the development of wrinkles (Harrison et al., 2018a). Preliminary numerical tests at different velocities suggested that velocity scaling beyond 300x would begin to inhibit the growth of wrinkles in the current simulations. Under these conditions, simulation times of around 12 to 15 hours (depending on material properties, use of stiffness damping and the point at which the simulation failed) using 48 cores were typical. Viscous damping was added to simulations using mass-proportional Rayleigh damping; a coefficient of 30 s^{-1} was used for the beam elements and 1000 s^{-1} for the upper blank holder. In some cases, use of stiffness-proportional Rayleigh damping (~$2x10^{-7}$ s) was required to improve numerical robustness, see Section 26.1.1 of (*Abaqus Analysis User's Guide 6.14*, n.d.). The positions of the die and lower blank holder were fixed while the upper blank holder was free to move only in the vertical direction (all other translational and rotational directions were fixed). The body force acting on the upper blank holder was 0.786kg x -9.81ms^{-2} = -7.71N. The punch was moved down in the *z*-direction at a constant rate, to cover a target distance of 80mm in 0.8s (i.e. 100mm.s^{-1}). The basic tooling setup is shown in Figure 9a.

In the absence of any perturbations, the dominant wrinkles in all four quadrants of the blank (see Figure 5) were always predicted to grow upwards. Downward wrinkle growth (see Figure 6) had to be artificially provoked in a manner analogous to the perturbations applied by hand in the experiments. To do this, rigid body spheres measuring 12mm in diameter were positioned

above the fabric, 65mm from the centre of the blank along the bias directions of the blank, and were used to push the blank downwards by 3mm during the early stage of the simulation (see Figure 9). The spheres were retracted once the punch reached 30mm travel depth, allowing subsequent unimpeded wrinkle growth with no further interference from the spheres.
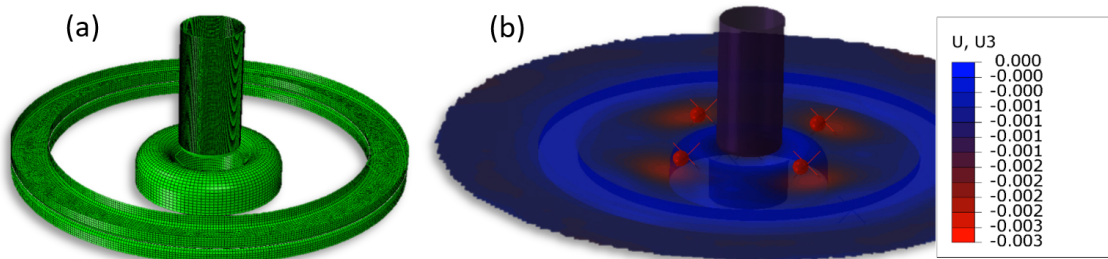

Figure 9. *(a) Rigid body tooling setup used in numerical simulations showing both upper and lower blank holders. Dimensions are given in Section 2.2. (b) Initial stage of a forming simulation designed to generate inverse wrinkles (downward depressions). Four spheres places over the bias direction of the fabric are used to create 3mm depressions during the early stage of the simulation. Here the blank is made translucent to reveal the relative position of the die under the blank. Legend in m.*

3.1 ROBUSTNESS OF SIMULATION APPROACH

The eight forming cases can be used to test the robustness of the simulation approach. The final prediction of each simulation, prior to numerical error (excessive rotation at a node) is shown in Figures 10(a-d) and 11(a-d). Only one simulation managed to reach the imposed 80mm draw depth without error (see Figure 11c). The final punch travel distance for each case is provided in the relevant figure caption, the colour legend indicates the vertical displacement of the blank surface profile (units in m). In three simulations (Figures 10c, 11a & 11c) some wrinkles changed their growth direction at large punch depths via an elastic 'snap-through' type behaviour. Similar wrinkle reversal was occasionally observed to occur in experiments, though not by snap through, but by the lateral encroachment of faster growing bulges or depressions. Also, the draw-in of the fabric sometimes became notably asymmetric towards the later stages of the simulation (see Figures 10c and 11c). Various parameters influenced the point at which numerical error occurred. Aside from the measured material behaviour and boundary conditions which are inherently fixed by the experiments, other parameters such as Rayleigh

damping (both mass and stiffness damping), length of the hinge elements, use of fully or reduced integrated membrane elements and the amount of velocity scaling, all affect the robustness of the simulations. In some cases, the simulations were able to predict extreme wrinkling behaviour and draw-in of the wrinkles down into the die (see, for example, Figure 12), though numerical error was not always directly connected to the severity of the wrinkling in the blank. These results highlight the need to evaluate not just the accuracy of forming simulations, but also their robustness. The latter is rarely discussed in the literature but is nevertheless an important consideration in evaluating the performance of a given modelling approach. Many forming codes will encounter numerical error under certain situations, depending on for example, the degree of deformation, the fabric's mechanical behaviour and damping values used in the simulation; the current experimental setup is designed to explore these limits of computational robustness.
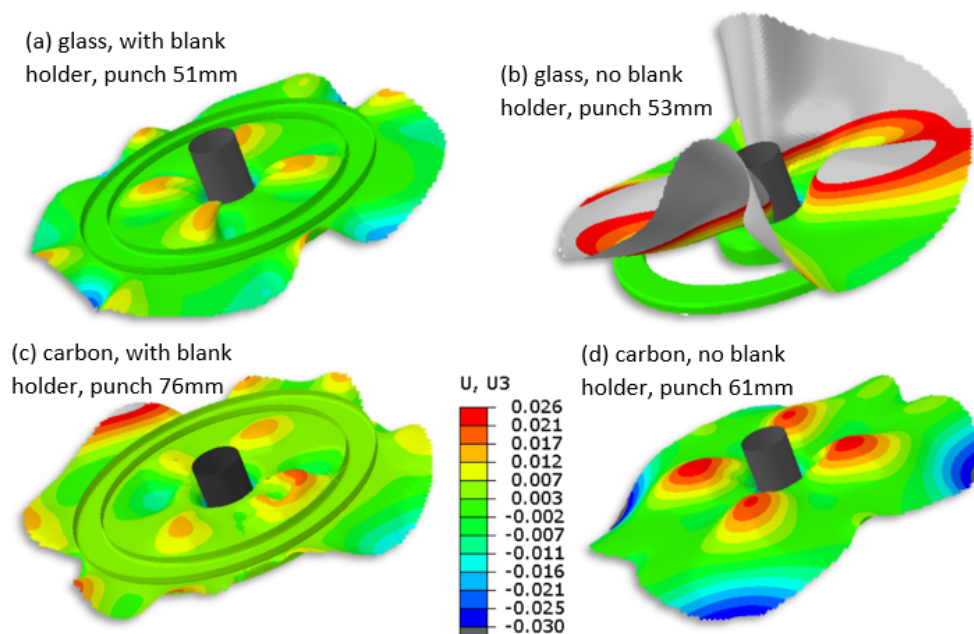

Figure 10. *Four deep draw forming cases for upward wrinkles (bulges), each at the final stage of the simulation prior to numerical error. The final punch displacement is indicated in the figure. The colour legend shows the vertical displacement of the blank's surface (in m).*
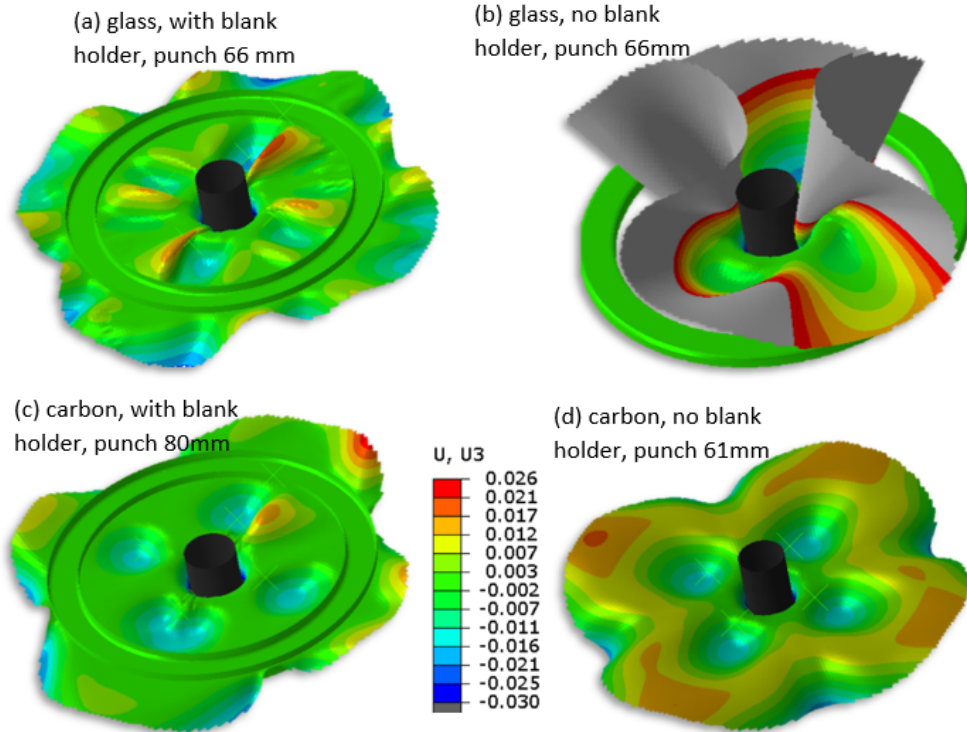
Figure 11. *Four deep draw forming cases for downward wrinkles (depressions), each at the final stage of the simulation prior to numerical error. The final punch displacement is indicated in the figure. The colour legend shows the vertical displacement of the blank's surface (in m).*
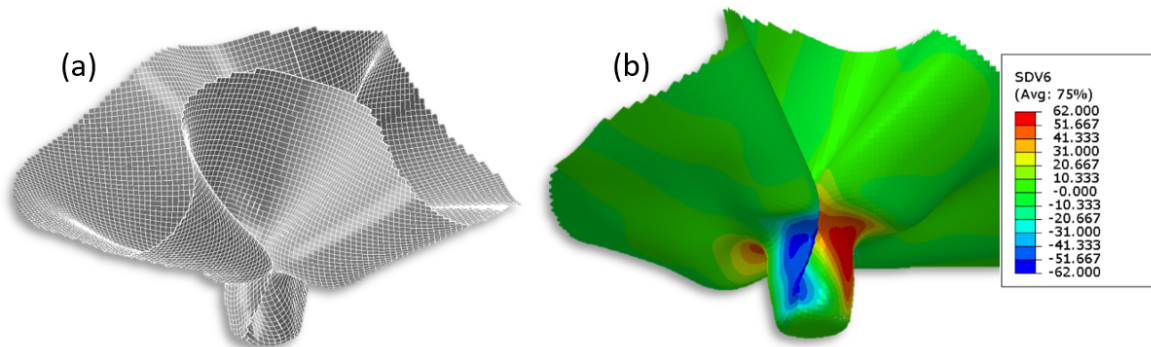

Figure 12. *Example of severe wrinkle drawn down into the die for case of glass with no upper blank holder, for downward growing wrinkles (depression). The lower blank holder and die are both hidden from view. (a) fibre directions indicated by the visible beams elements (white lines) and (b) shear angle indicated by the colour legend. Punch depth = 66mm.*

4 COMPARISON OF EXPERIMENTS AND SIMULATIONS USING DIGITAL SCAN DATA

Digitising the surface morphology of the deformed blanks allows more detailed comparison of the experiments and simulations. Both SLS (see Section 2.4.1) and photogrammetry (see Section 2.4.2) were used to record the surface profile of the blank. Figures 13 and 14 show full field comparisons of the numerical predictions and the experimental measurements (here using just the SLS scanning data which proved to be the more accurate of the two scanning methods, see Section 4.2). The colour legend in each image indicates the vertical height of the surface (in mm). Experimental scanning produced a much denser point cloud than simulations, data points in the latter are provided by nodal positions. This is evident in Figure 13 and 14, though the simulation data is still sufficiently dense to permit scrutiny and comparison of results.
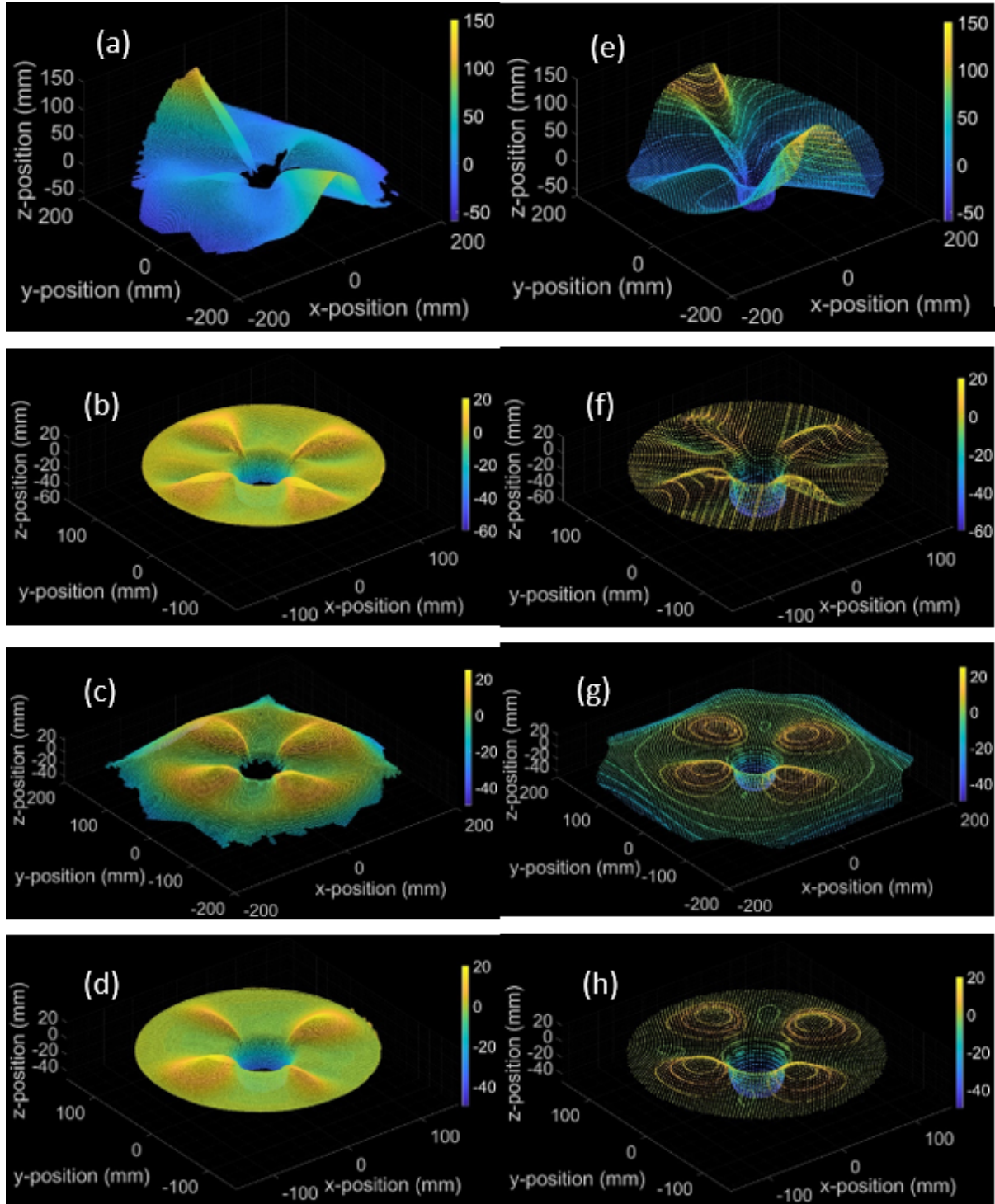
Figure 13. *Isometric views of experiments (left) and simulations (right) for **first series of tests, i.e.** **upward growing wrinkles**: (a) & (e) glass fabric without blank-holder, punch depth=50mm, (b) & (f) glass fabric with blank-holder, punch depth=50mm, (c) & (g) carbon fabric without blank-holder, punch depth=40mm, (d) & (h) carbon fabric with blank-holder, punch depth=40mm.*

Figure 14. *Isometric views of experiments (left) and simulations (right) for **second series of tests, i.e.** **downward growing wrinkles**: (a) & (e) glass fabric without blank-holder, punch depth=40mm, (b) & (f) glass fabric with blank-holder, punch depth=60mm, (c) & (g) carbon fabric without blank-holder, punch depth=40mm, (d) & (h) carbon fabric with blank-holder, punch depth=40mm.*
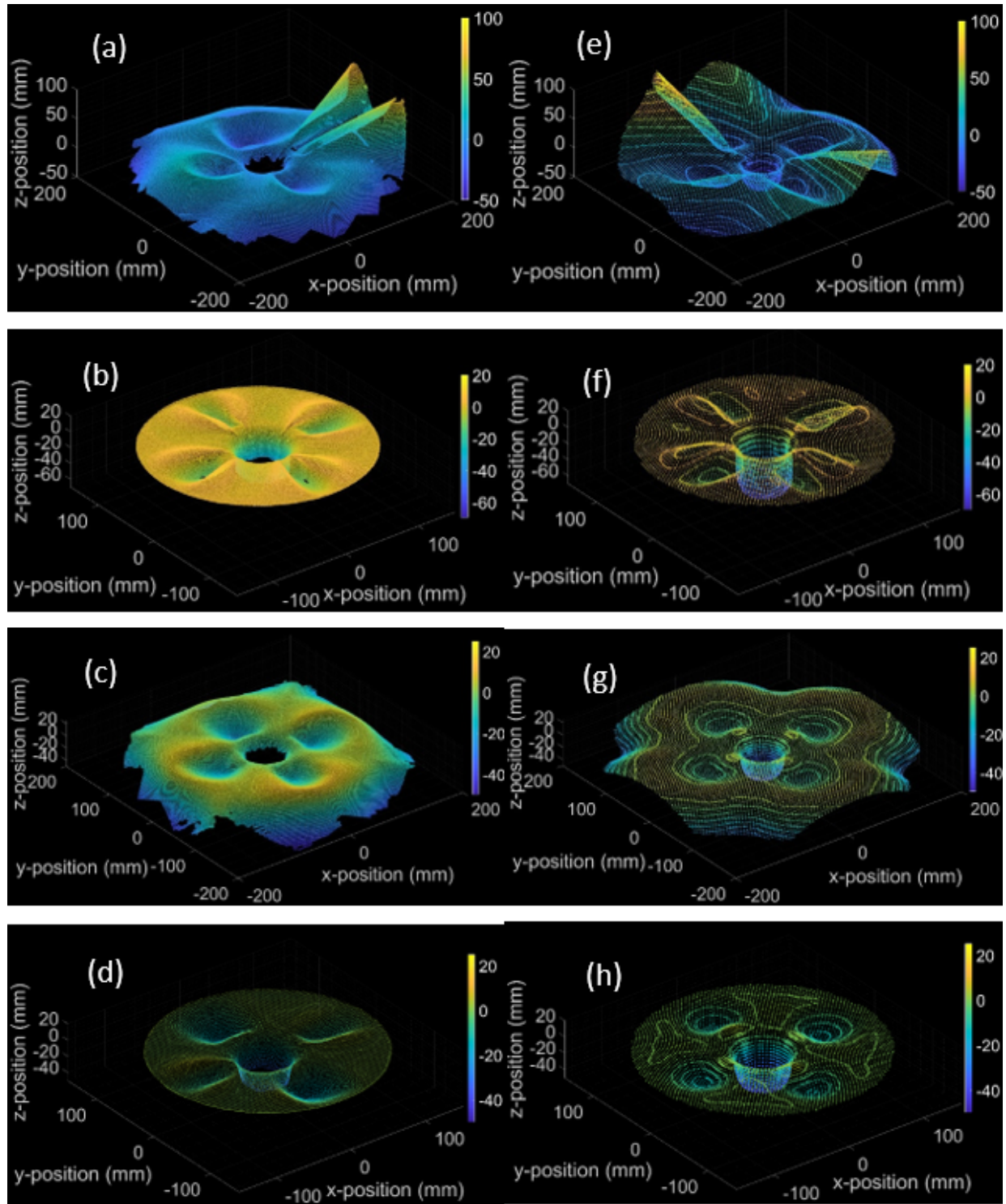
4.1 EXPERIMENT REPEATABILITY

Prior to drawing comparison between experiments and simulations, the repeatability of the experiments was examined. Three repeat tests were conducted for each experiment in the first series of tests (upward growing bulges) under the four different experimental conditions, i.e. forming both glass and carbon fabrics, both with and without the upper blank holder in place. The results of the polar plots of angular position versus wrinkle height, measured using the SLS and generated using the process described in Section 2.6 (to produce the outer ring profile displayed in Figure 7), are shown here in Figure 15. The experiments generally show good repeatability with the glass fabric without blank holder, Figure 15a, being the most variable case.
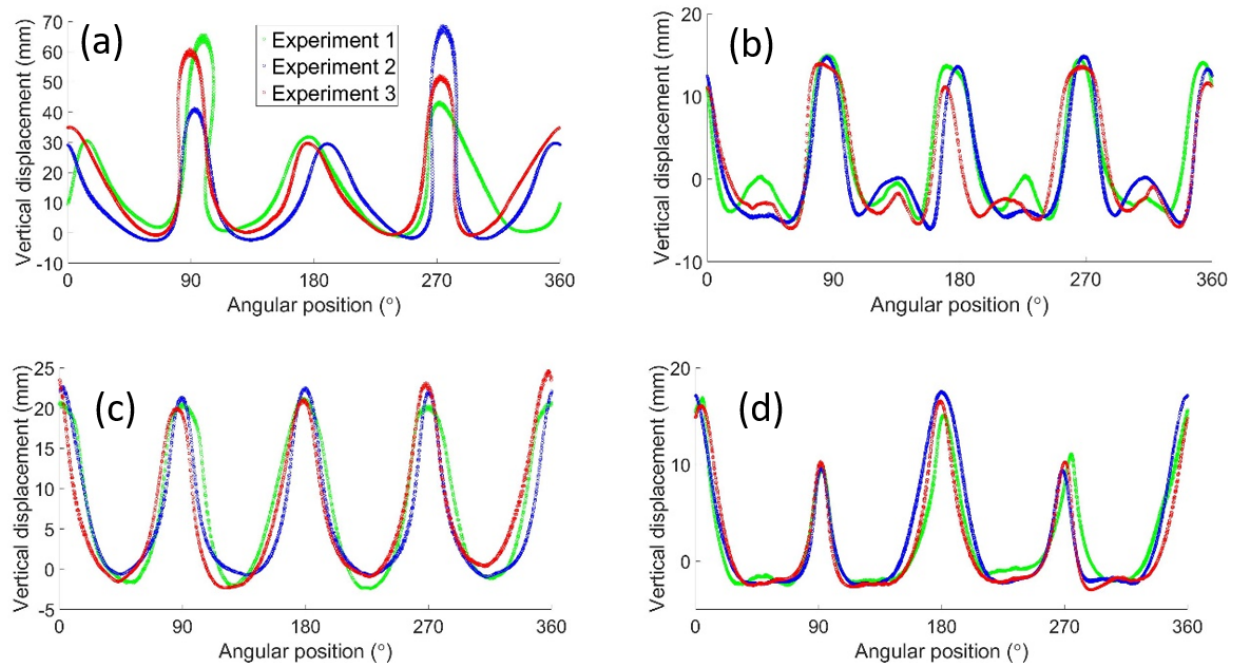

Figure 15. *Three repeat tests showing angular position versus wrinkle height measured using the SLS for the **first series of tests** (bulges): (a) glass fabric without blank holder at r=87+/-2mm & punch depth = 50mm, (b) glass fabric with blank holder at r=77+/-2mm & punch depth = 50mm, (c) carbon fabric without blank holder at r=74+/-2mm & punch depth = 40mm and (d) carbon fabric with blank holder at r=70+/-2mm & punch depth = 40mm.*

4.1.1 Predicted versus Measured Wrinkle Height in Flange Region for Upward Growing Wrinkles

Comparison of the polar plots of angular position versus wrinkle height, as predicted in both numerical simulations and measured in the first series of tests, are shown in Figure 16.

Experimental results are generated from full field scans performed using both SLS and photogrammetry techniques. The two techniques show reasonably good agreement with each other (blue and green points) though, as will be explained in Section 4.2, the SLS results are likely to be the more accurate of the two.
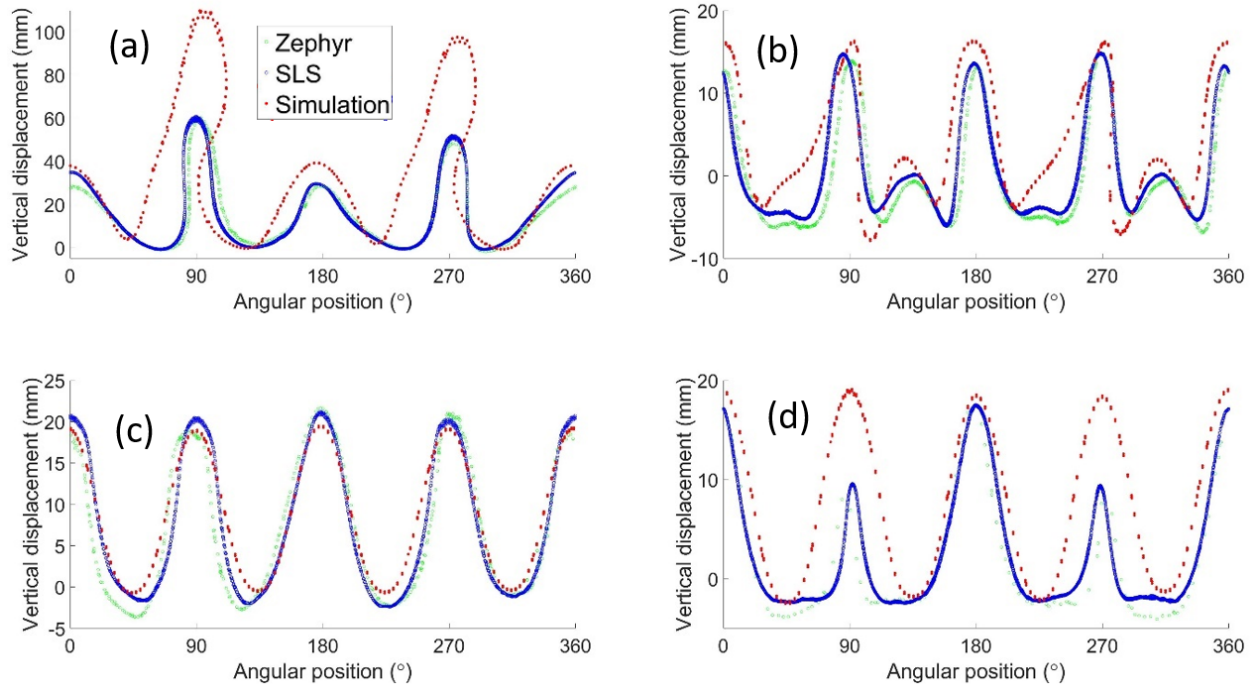

*Figure 16. Comparison of angular position versus wrinkle height predicted by simulations and measured using both SLS and Zephyr (photogrammetry) for the **first series of tests** (bulges): (a) glass fabric without blank holder at r=87+/-2mm & punch depth = 50mm, (b) glass fabric with blank holder at r=77+/-2mm & punch depth = 50mm, (c) carbon fabric without blank holder at r=74+/-2mm & punch depth = 40mm and (d) carbon fabric with blank holder at r=70+/-2mm & punch depth = 40mm.*

The form and amplitude of the wrinkles undergo peculiar changes depending on the fabric type and the boundary conditions of the test. The case of glass fabric without a blank holder (Figure 16a) produced by far the largest wrinkles in this series of experiments (note the larger vertical scale in Figure 16a compared to Figures 16b-d) with two large and two relatively small wrinkles occurring in diagonally opposed quadrants of the blank. The corresponding simulations also predict two different wrinkle amplitudes but significantly overpredict the size of the large wrinkles while closely predicting the smaller wrinkles. The wrinkle amplitude is significantly reduced by adding the upper blank holder to the glass fabric in the next case (Figure 16b). Here the amplitude of the dominant wrinkles is constant in all quadrants with two additional minor

wrinkles emerging between the four dominant ones. The simulations predict this unusual behaviour quite well. The case of the carbon fabric without a blank holder (Figure 16c) produces four equal sized wrinkles in each quadrant of the blank and the simulations predict the form and amplitude of these wrinkles very well. Surprisingly, adding the upper blank holder to the carbon fabric (Figure 16d) leads to a reduction in the amplitude of just two of the wrinkles while the amplitude of the other two wrinkles remains almost unchanged. The simulation predicts the amplitude of the two larger wrinkles very well but fails to predict the decrease in amplitude of the two smaller wrinkles. Overall, the simulations perform quite well in predicting the wrinkles in the four cases.

4.1.2 Predicted versus Measured Wrinkle Height in Flange Region for Downward Growing Wrinkles

In the second series of experiments, depressions rather than bulges were created in the four quadrants of the blank. To recreate this behaviour in simulations, perturbations were induced in the blank during the early stages for the forming process (see Section 3). Comparison of the polar plots of angular position versus wrinkle height, as predicted in both numerical simulations and measured in the second series of tests, are shown in Figure 17.
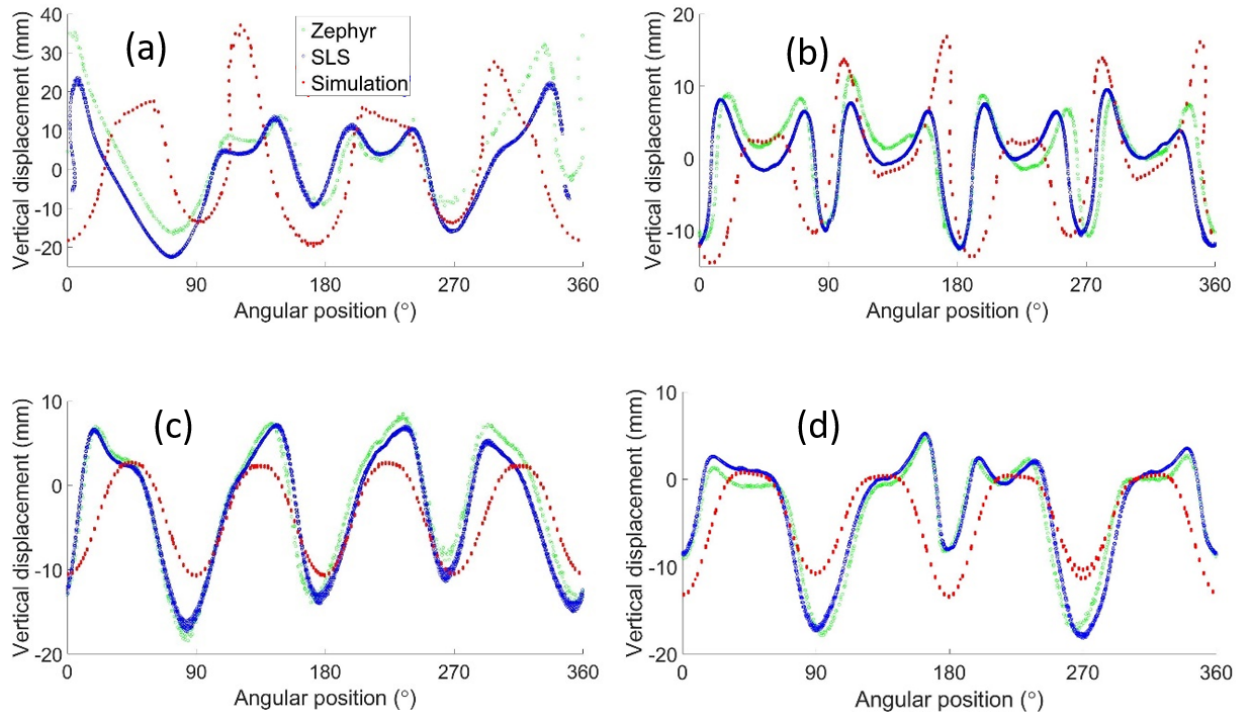
Figure 17. Comparison of angular position versus wrinkle height predicted by simulations and measured using both SLS and Zephyr (photogrammetry) for the **second series of tests** (depressions): (a) glass fabric without blank holder at r=80+/-2mm & punch depth = 40mm, (b) glass fabric with blank holder at r=76+/-2mm & punch depth = 60mm, (c) carbon fabric without blank holder at r=92+/-2mm & punch depth = 40mm and (d) carbon fabric with blank holder at r=**+/-2mm & punch depth = 40mm.

In each case, as expected, four deep depressions rather than bulges are created around the blank, though in some cases the detailed profile of the blank between the depressions takes on unusual shapes. In Figure 17a, i.e. glass without upper blank holder, two of these inter-depression peaks have a single peaked profile while the other two show two smaller peaks. This behaviour is more exaggerated in Figure 17b, i.e. glass with upper blank holder, with two distinct peaks occurring in all four inter-depression regions. The simulations perform reasonably well in recreating the complex form of the wrinkles for both experiments with the glass fabric. The carbon fabric without the blank holder produces much smaller depressions than the glass (compare Figures 17a and 17c, noting the difference in vertical scale), with the peak to trough amplitude about half that of the glass fabric. The simulations capture this change reasonably well though the predicted amplitude is about 40% lower than that measured in the experiments. When the blank holder is added to the carbon fabric the peak to trough amplitude is decreased slightly and the peaks become truncated. In one quadrant, the peak changes from a single to a double peak profile. The simulations again underpredict the peak to trough amplitude by around 40% and in this case do not predict double peak profiles but do predict a slight truncation of the top of the peaks.

4.1.3 Analysing Wrinkle Draw-In

Section 4.1.1 and 4.1.2 demonstrate how the form of a wrinkle can grow either upwards or downwards and can be predicted reasonably well by simulations. From a practical point of view, it is useful to know whether the direction of wrinkle growth makes wrinkle draw-in more or less likely. To investigate this question, the form of the blank as it draws down inside the interior of the die, i.e. the form of the inner green ring shown in Figure 7 when viewed from above, is examined for both upward and downward growing wrinkles at specified punch depths. Polar plots of angle versus the (*x,y*) position of the blank are shown in Figures 18 and 19. In the absence of wrinkling, the blank will slide into the die hole, pulled tight against the die

wall due to the tension created by friction acting between the die and the blank. In this case, the inner green ring shown in Figure 7 would be circular, i.e. it would conform with the shape of the inside of the die. However, if wrinkles were to be pulled into the die, the blank would no longer stay close to the die wall and the inner green ring would lose its circular profile. Figure 18 shows the form of the blank at different punch depths for **the first series of experiments and simulations, i.e. for upward growing wrinkles**. The blue points are experimental measurements, the red points are predictions (note that Figure 18a has few experimentally measured points as the large wrinkles of the blank obscured much of the inner region of the die from the scanner). Figure 19 shows the same information but for **the second series of experiments and simulations, i.e. for downward growing wrinkles**. Details of each experiment are provided in the caption, including punch travel depth. The main point to note in comparing Figures 18 and 19 is that wrinkle draw-in measured in experiments is significantly reduced when downward growing wrinkles are present in the blank. This is evidenced by the more circular form of the blue data points in Figure 19 compared to Figure 18. The 'inward bumps' that signify wrinkles being drawn-into the die are apparent in each quadrant of the polar plots of Figure 18 but are almost entirely absent from Figure 19. The simulations perform moderately well in predicting the wrinkle draw-in. In Figure 18a (glass fabric with no blank holder) a large wrinkle is drawn down into the die, signified by the clear inward projections for both experimental and predicted data. The predicted data also show some evidence of wrinkle draw-in in Figure 18b (glass fabric with blank holder), though the less numerous data points obtained from simulations, limited by the number of nodes, makes visualisation of wrinkle draw-in less clear. Wrinkle draw-in is also apparent for the experimental data in Figures 18c-d (the two carbon fabric scenarios, without and with blank holder), though is not evident in the predicted data.
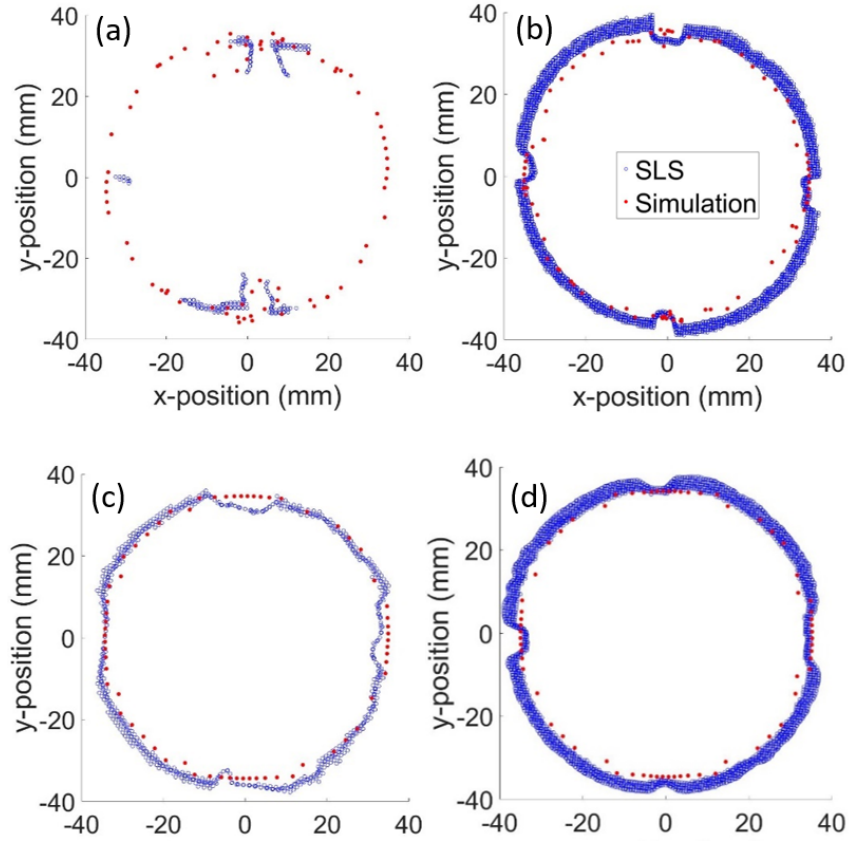
Figure 18. Plan view of simulation and experimental cloud points of the **first series of tests (bulges),** falling within 'collection volume' shown in Figure 8, for: (a) glass fabric without blank holder, punch depth = 50mm, (b) glass fabric with blank holder, punch depth = 50mm, (c) carbon fabric without blank holder, punch depth = 40mm, (d) carbon fabric with blank holder, punch depth = 40mm.

For the second series of experiments involving downward growing wrinkles, the experiments involving the glass fabric were stopped when the wrinkle first started to draw into the die. For the glass fabric without a blank holder, Figure 19a, this occurred at a punch depth of about 40mm. The slightly non-circular form of the experimental and numerical data in Figure 19a both indicate some degree of wrinkle draw-in at that point. Figure 19b, glass fabric with blank holder reached a depth of about 60mm before the test was stopped. The plot shows relatively little sign of wrinkle draw-in compared to Figure 18b despite being drawn to a deeper depth (60mm versus 50mm), though the simulation data does indicate the beginnings of wrinkle draw-in. Figures 19c and 19, the carbon fabric without and with blank holder are produced at the same

draw depth as Figures 18c and 18d but are clearly less affected by wrinkle draw-in; both the experimental and numerical data create almost perfectly circular plots in Figures 19c and 19d.
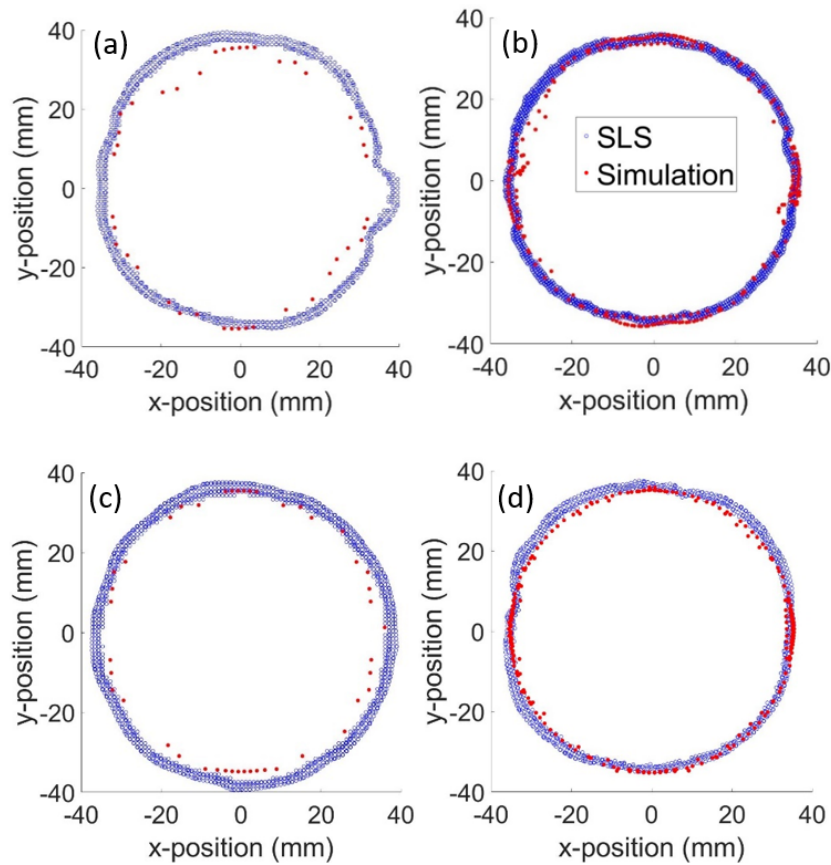

*Figure 19. Plan view of simulation and experimental cloud points of the **second series of tests** **(depressions),** falling within 'collection volume' shown in Figure 8, for: (a) glass fabric without blank holder, punch depth = 40mm, (b) glass fabric with blank holder, punch depth = 60mm, (c) carbon fabric without blank holder, punch depth = 40mm, (d) carbon fabric with blank holder, punch depth = 40mm.*

The data in this section provide clear evidence that the direction of wrinkle growth strongly influences the degree of wrinkle draw-in. This observation is less relevant to preforming of engineering fabrics (Nosrat Nezami et al., 2017) or even thermosetting prepregs (Lin et al., 2007), where full blank holders can be used to mitigate wrinkling. In contrast, forming of pre-consolidated advanced thermoplastic sheets is sometimes most easily accomplished using either tensioning springs (Chen et al., 2015; Harrison et al., 2013) or a rubber diaphragm (McGuinness and ÓBrádaigh, 1995; O'Brádaigh et al., 1991), due to the requirement to melt the entire blank prior to forming. In these setups, the blank is relatively unconstrained and wrinkles can grow in any direction. One approach to mitigating wrinkling in these cases could

be to direct the wrinkles downwards during the forming process (various methods of doing this can be imagined), such that the wrinkles are 'ironed out' rather than being drawn into the usable region of the formed part.

4.2   EVALUATION OF SCANNING APPROACHES

The experimental setup described in this paper is proposed as a reliable technique to accurately characterise fabric wrinkling during the deep draw process. It is useful to consider the suitability of the two different scanning methods employed to digitise the surface shape of the forming blank. Overall, for precision and accuracy, the SLS system was better than the 3DF Zephyr photogrammetry technique. While collecting photogrammetry images was easier than using the SLS, the subsequent data analysis was much more difficult. Accurate pre-experiment calibration of the SLS automatically provided scans of the correct scale (in mm) and design of the turntable setup (with well-defined 45° rotational increments), made fusion of the images easy. In contrast, finding the correct scale and alignment for fusion of the photogrammetry results was more difficult (in this investigation the SLS scans were used to determine the scale for the photogrammetry results). Figure 20 shows a direct visual comparison of scans made using the two technologies, together with an equivalent simulation prediction. The David SLS software tends to produce a finer mesh; the wrinkles are slightly sharper. However, due to restrictions on the positioning of the SLS projector, the photogrammetry results could create a more complete mesh, including the inside of the die (with the punch removed) and with appropriate care and effort, good quality photogrammetry results were possible, see for example, Figures 16 and 17. Given the much lower cost of the photogrammetry option, it remains a viable solution for digitising results, albeit requiring greater time and effort to avoid introduction of unwanted errors during post-processing of results.
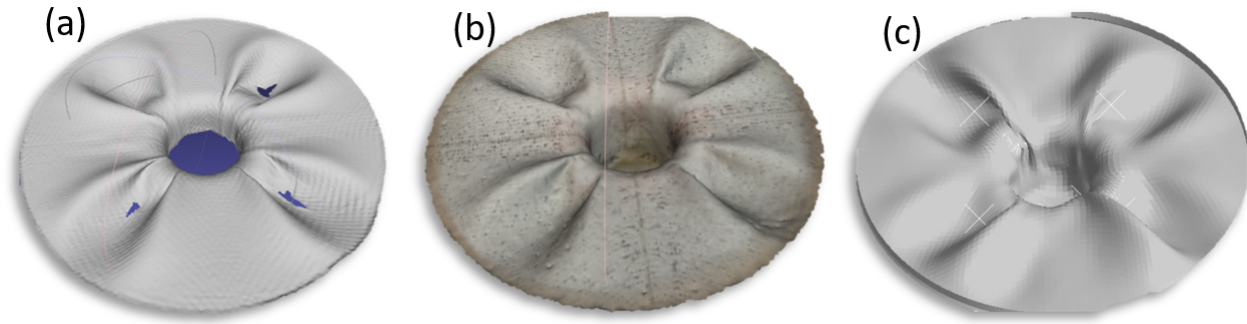
Figure 20. Example of forming experiment recorded with punch removed: (a) the DAVID-SLS system, (b) Zephyr photogrammetry system and (c) simulation result. Punch depth = 60mm for glass fabric with blank holder and downward wrinkles (depressions).

5 CONCLUSIONS

An experimental method of accurately characterising the wrinkling mechanics of engineering fabrics has been demonstrated. Digitising the form of the surface of the deformed blank facilitates direct comparison of experimental measurements and numerical predictions via polar plots. The accuracy of the simulation approach was found to be good and able to distinguish the forming behaviours of the two different fabrics. However, comparison with experiments suggested the predictions for the glass fabric were overly stiff. For example, Figure 16a shows the glass fabric wrinkle amplitude to be significantly higher than experimentally measured values. A plausible reason for this is the constant values used for the bending (out and in-plane) and torsional stiffnesses in the model. Previous detailed experimental investigations have shown that the out-of-plane bending stiffness can decrease significantly with increasing bend curvature (de Bilbao et al., 2010; Yu et al., 2020), the same is likely to be true for in-plane and torsional stiffnesses; a detail omitted in the current model (though this is something that might be implemented in future). The numerical simulations were found to be reasonably robust, in some cases predicting extreme wrinkle draw-in, though numerical stiffness-related damping had to be introduced in some cases to reach deeper punch travel depths. The main drawback of this modelling approach is its high computational cost due to the use of hinge connector elements. Current simulation times make the method more suitable for scientific investigation rather than as a viable computational design optimisation tool.

An interesting experimental observation was the stochastic nature of the direction of wrinkle growth. This contrasts with simulations, which always predicted wrinkles to grow in the same upward direction, unless forced to do otherwise. The ability to manipulate the direction of wrinkle growth by introducing an initial perturbation during the early stages of growth was demonstrated in both experiments and simulations. Furthermore, the direction of wrinkle growth was shown to strongly influence the degree of wrinkle draw-in; downward growing wrinkles were effectively ironed flat when entering the die, mitigating the onset of wrinkle draw-in until the punch reached relatively deep travel depths. It is suggested that this observation might be used to reduce the severity of wrinkle draw-in during actual forming processes. For example, forming setups using tensioning springs (Chen et al., 2015; Harrison et al., 2013) or double diaphragms (McGuinness and ÓBrádaigh, 1995; O'Brádaigh et al., 1991) could be specifically designed to reduce wrinkle draw-in by controlling the direction of wrinkle growth during the forming process.

Acknowledgments

REFERENCES

Abaqus Analysis User's Guide 6.14, n.d.

Abdiwi, F., Harrison, P., Koyama, I., Yu, W.R., Long, A.C., Corriea, N., Guo, Z., 2012. Characterising and modelling variability of tow orientation in engineering fabrics and textile composites. Compos. Sci. Technol. 72, 1034–1041. https://doi.org/10.1016/j.compscitech.2012.03.017

Abdiwi, F., Harrison, P., Yu, W.R., 2013. Modelling the Shear-Tension Coupling of Woven Engineering Fabrics. Adv. Mater. Sci. Eng. 2013, 1–9.

Aimene, Y., Vidal-Salle, E., Hagege, B., Sidoroff, F., Boisse, P., 2010. A Hyperelastic Approach for

Composite Reinforcement Large Deformation Analysis. J. Compos. Mater. 44, 5–26. https://doi.org/10.1177/0021998309345348

Alsayednoor, J., Harrison, P., Yu, W.R., 2017. Influence of specimen pre-shear and wrinkling on the accuracy of uniaxial bias extension test results. Compos. Part A Appl. Sci. Manuf. 101, 81–97. https://doi.org/10.1016/j.compositesa.2017.06.006

Boisse, P., Gasser, A., Hivet, G., 2001. Analyses of fabric tensile behaviour: Determination of the biaxial tension-strain surfaces and their use in forming simulations. Compos. - Part A Appl. Sci. Manuf. 32, 1395–1414. https://doi.org/10.1016/S1359-835X(01)00039-2

Boisse, P., Hamila, N., Vidal-Salle, E., Dumont, F., 2011. Simulation of wrinkling during textile composite reinforcement forming. Influence of tensile, in-plane shear and bending stiffnesses. Compos. Sci. Technol. 71, 683–692. https://doi.org/10.1016/j.compscitech.2011.01.011

Breuer, U., Neitzel, M., Ketzer, V., Reinicke, R., 1996. Deep drawing of fabric-reinforced thermoplastics: Wrinkle formation and their reduction. Polym. Compos. 17, 643–647. https://doi.org/10.1002/pc.10655

Buet-Gautier, K., Boisse, P., 2001. Experimental analysis and modeling of biaxial mechanical behavior of woven composite reinforcements. Exp. Mech. 41, 260–269. https://doi.org/10.1007/BF02323143

Bussetta, P., Correia, N., 2018. Numerical forming of continuous fibre reinforced composite material: A review. Compos. Part A Appl. Sci. Manuf. 113, 12–31. https://doi.org/10.1016/j.compositesa.2018.07.010

Cao, J., Akkerman, R., Boisse, P., Chen, J., Cheng, H.S., de Graaf, E.F., Gorczyca, J.L., Harrison, P., Hivet, G., Launay, J., Lee, W., Liu, L., Lomov, S. V., Long, A., de Luycker, E., Morestin, F., Padvoiskis, J., Peng, X.Q., Sherwood, J., Stoilova, T., Tao, X.M., Verpoest, I., Willems, A., Wiggers, J., Yu, T.X., Zhu, B., 2008. Characterization of mechanical behavior of woven fabrics: Experimental methods and benchmark results. Compos. Part A Appl. Sci. Manuf. 39, 1037–1053. https://doi.org/10.1016/j.compositesa.2008.02.016

Chen, S., Harper, L.T., Endruweit, A., Warrior, N.A., 2015. Composites : Part A Formability optimisation of fabric preforms by controlling material draw-in through in-plane constraints. Compos. PART A 76, 10–19. https://doi.org/10.1016/j.compositesa.2015.05.006

Chen, Z.R., Ye, L., 2006. A micromechanical compaction model for woven fabric preforms. Part II: Multilayer. Compos. Sci. Technol. 66, 3263–3272. https://doi.org/10.1016/j.compscitech.2005.07.010

Cooper, D.N.E., 1960. The Stiffness of Woven Textiles. J. Text. Inst. Trans. 51, T317–T335. https://doi.org/10.1080/19447026008659775

Costantini, R., Lennard, F., Alsayednoor, J., Harrison, P., 2020. Investigating mechanical damage mechanisms of tapestries displayed at different angles using 2D DIC. Eur. Phys. J. Plus 123,

1–17.

Creech, G., Pickett, A.K., 2006. Meso-modelling of Non-crimp Fabric composites for coupled drape and failure analysis. J. Mater. Sci. 41, 6725–6736. https://doi.org/10.1007/s10853-006-0213-6

D'Agostino, M. V., Giorgio, I., Greco, L., Madeo, A., Boisse, P., 2015. Continuum and discrete models for structures including (quasi-) inextensible elasticae with a view to the design and modeling of composite reinforcements. Int. J. Solids Struct. 59, 1–17. https://doi.org/10.1016/j.ijsolstr.2014.12.014

De Angelo, M., Barchiesi, E., Giorgio, I., Abali, B.E., 2019. Numerical identification of constitutive parameters in reduced-order bi-dimensional models for pantographic structures: application to out-of-plane buckling. Arch. Appl. Mech. 89, 1333–1358. https://doi.org/10.1007/s00419-018-01506-9

de Bilbao, E., Soulat, D., Hivet, G., Gasser, A., 2010. Experimental Study of Bending Behaviour of Reinforcements. Exp. Mech. 50, 333–351. https://doi.org/10.1007/s11340-009-9234-9

de Bilbao, E., Soulat, D., Hivet, G., Launay, J., Gasser, A., 2008. Bending test of composite reinforcements. Int. J. Mater. Form. 1, 835–838. https://doi.org/10.1007/s12289-008-0265-z

Dell'Isola, F., Steigmann, D., 2014. A Two-Dimensional Gradient-Elasticity Theory for Woven Fabrics. J. Elast. 118, 113–125. https://doi.org/10.1007/s10659-014-9478-1

Ferretti, M., Madeo, A., dell'Isola, F., Boisse, P., 2014. Modeling the onset of shear boundary layers in fibrous composite reinforcements by second-gradient theory. Zeitschrift fur Angew. Math. und Phys. 65, 587–612. https://doi.org/10.1007/s00033-013-0347-8

Gatouillat, S., Bareggi, A., Vidal-Salle, E., Boisse, P., 2013. Meso modelling for composite preform shaping - Simulation of the loss of cohesion of the woven fibre network. Compos. Part A Appl. Sci. Manuf. 54, 135–144. https://doi.org/10.1016/j.compositesa.2013.07.010

Gereke, T., Döbrich, O., Hübner, M., Cherif, C., 2013. Experimental and computational composite textile reinforcement forming: A review. Compos. Part A Appl. Sci. Manuf. 46, 1–10. https://doi.org/10.1016/j.compositesa.2012.10.004

Giorgio, I., 2016. Numerical identification procedure between a micro-Cauchy model and a macro-second gradient model for planar pantographic structures. Zeitschrift für Angew. Math. und Phys. 67, 95. https://doi.org/10.1007/s00033-016-0692-5

Giorgio, I., Della Corte, A., Dell'Isola, F., Steigmann, D.J., 2016. Buckling modes in pantographic lattices. Comptes Rendus Mécanique. https://doi.org/10.1016/j.crme.2016.02.009

Giorgio, I., Harrison, P., Dell'Isola, F., Alsayednoor, J., Turco, E., 2018. Wrinkling in engineering fabrics: A comparison between two different comprehensive modelling approaches. Proc. R. Soc. A Math. Phys. Eng. Sci. 474. https://doi.org/10.1098/rspa.2018.0063

Hancock, S.G., Potter, K.D., 2006. The use of kinematic drape modelling to inform the hand lay-

up of complex composite components using woven reinforcements. Compos. Part A Appl. Sci. Manuf. 37, 413–422. https://doi.org/10.1016/j.compositesa.2005.05.044

Harrison, P., 2016. Modelling the forming mechanics of engineering fabrics using a mutually constrained pantographic beam and membrane mesh. Compos. Part A Appl. Sci. Manuf. 81, 145–157. https://doi.org/10.1016/j.compositesa.2015.11.005

Harrison, P., Abdiwi, F., Guo, Z., Potluri, P., Yu, W.R., 2012. Characterising the shear-tension coupling and wrinkling behaviour of woven engineering fabrics. Compos. Part A Appl. Sci. Manuf. 43, 903–914. https://doi.org/10.1016/j.compositesa.2012.01.024

Harrison, P., Alvarez, M.F., Anderson, D., 2018a. Towards comprehensive characterisation and modelling of the forming and wrinkling mechanics of engineering fabrics. Int. J. Solids Struct. 154, 2–18. https://doi.org/10.1016/j.ijsolstr.2016.11.008

Harrison, P., Gomes, R., Curado-Correia, N., 2013. Press forming a 0/90 cross-ply advanced thermoplastic composite using the double-dome benchmark geometry. Compos. Part A Appl. Sci. Manuf. 54, 56–69. https://doi.org/10.1016/j.compositesa.2013.06.014

Harrison, P., Hartel, F., 2016. Erratum: "Evaluation of normalisation methods for uniaxial bias extension tests on engineering fabrics" (Composites: Part A (2016) 80 (104-106)). Compos. Part A Appl. Sci. Manuf. 80, 104–106. https://doi.org/10.1016/j.compositesa.2015.10.013

Harrison, P., Taylor, E., Alsayednoor, J., 2018b. Improving the accuracy of the uniaxial bias extension test on engineering fabrics using a simple wrinkle mitigation technique. Compos. Part A 108, 53–61. https://doi.org/10.1016/j.compositesa.2018.02.025

Harrison, P., Wiggers, J., Long, A.C., 2008. Normalization of Shear Test Data for Rate-independent Compressible Fabrics. J. Compos. Mater. 1–30. https://doi.org/10.1177/0021998308095367

Harrison, P., Wiggers, J., Long, A.C., 2007. Normalisation Of Shear Test Data for Rate-Independent Compressible Fabric. AIP Conf. Proc. 907, 1011–1016. https://doi.org/10.1063/1.2729646

Harrison, P., Yu, W.R., Long, A.C., 2011. Rate dependent modelling of the forming behaviour of viscous textile composites. Compos. Part A Appl. Sci. Manuf. 42, 1719–1726. https://doi.org/10.1016/j.compositesa.2011.07.026

Hosseini, A., Kashani, M.H., Sassani, F., Milani, A.S., Ko, F., 2017. A mesoscopic analytical model to predict the onset of wrinkling in plainwoven preforms under bias extension shear deformation. Materials (Basel). 10, 1–16. https://doi.org/10.3390/ma10101184

Hosseini, A., Kashani, M.H., Sassani, F., Milani, A.S., Ko, F.K., 2018. Identifying the distinct shear wrinkling behavior of woven composite preforms under bias extension and picture frame tests. Compos. Struct. 185, 764–773. https://doi.org/10.1016/j.compstruct.2017.11.033

Hu, J., 2004. Structure and mechanics of woven fabrics, 1st ed. Woodhead Publishing Limited, Cambridge. https://doi.org/10.1017/CBO9781107415324.004

ISO, B.E., 1998. Textiles — Test methods for nonwovens Part 7: Determination of bending length.

Iwata, A., Inoue, T., Naouar, N., Boisse, P., Lomov, S. V., 2019. Coupled meso-macro simulation of woven fabric local deformation during draping. Compos. Part A Appl. Sci. Manuf. 118, 267–280. https://doi.org/10.1016/j.compositesa.2019.01.004

Komeili, Milani, 2016. On effect of shear-tension coupling in forming simulation of woven fabric reinforcements. Compos. Part B Eng. 99, 17–29. https://doi.org/10.1016/j.compositesb.2016.05.004

Labanieh, A.R., Garnier, C., Ouagne, P., Dalverny, O., Soulat, D., 2018. Intra-ply yarn sliding defect in hemisphere preforming of a woven preform. Compos. Part A Appl. Sci. Manuf. 107, 432–446. https://doi.org/10.1016/j.compositesa.2018.01.018

Lammens, N., Kersemans, M., Luyckx, G., Van Paepegem, W., Degrieck, J., 2014. Improved accuracy in the determination of flexural rigidity of textile fabrics by the Peirce cantilever test (ASTM D1388). Text. Res. J. 84, 1307–1314. https://doi.org/10.1177/0040517514523182

Lin, H., Wang, J., Long, A.C., Clifford, M.J., Harrison, P., 2007. Predictive modelling for optimization of textile composite forming. Compos. Sci. Technol. 67, 3242–3252. https://doi.org/10.1016/j.compscitech.2007.03.040

Lomov, S. V., Verpoest, I., 2006. Model of shear of woven fabric and parametric description of shear resistance of glass woven reinforcements. Compos. Sci. Technol. 66, 919–933. https://doi.org/10.1016/j.compscitech.2005.08.010

Lomov, S. V., Verpoest, I., Barburski, M., Laperre, J., 2003. Carbon composites based on multiaxial multiply stitched preforms. Part 2. KES-F characterisation of the deformability of the preforms at low loads. Compos. Part A Appl. Sci. Manuf. 34, 359–370. https://doi.org/10.1016/S1359-835X(03)00025-3

McGuinness, G.B., ÓBrádaigh, C.M., 1995. Effect of preform shape on buckling of quasi-isotropic thermoplastic composite laminates during sheet forming. Compos. Manuf. 6, 269–280. https://doi.org/10.1016/0956-7143(95)95020-Y

Mercier, A.A., 1930. Coefficient of friction of fabrics. Bur. Stand. J. Res. 5, 243. https://doi.org/10.6028/jres.005.014

MeshLab, n.d.

Mulvihill, D.M., Smerdova, O., Sutcliffe, M.P.F., 2017. Friction of carbon fibre tows. Compos. Part A Appl. Sci. Manuf. 93, 185–198. https://doi.org/10.1016/j.compositesa.2016.08.034

Najjar, W., Pupin, C., Legrand, X., Boude, S., Soulat, D., Dal Santo, P., 2014. Analysis of frictional behaviour of carbon dry woven reinforcement. J. Reinf. Plast. Compos. 33, 1037–1047. https://doi.org/10.1177/0731684414521670

Nosrat-Nezami, F., Gereke, T., Eberdt, C., Cherif, C., 2014. Characterisation of the shear-tension

coupling of carbon-fibre fabric under controlled membrane tensions for precise simulative predictions of industrial preforming processes. Compos. Part A Appl. Sci. Manuf. 67, 131–139. https://doi.org/10.1016/j.compositesa.2014.08.030

Nosrat Nezami, F., Gereke, T., Cherif, C., 2017. Active forming manipulation of composite reinforcements for the suppression of forming defects. Compos. Part A Appl. Sci. Manuf. 99, 94–101. https://doi.org/10.1016/J.COMPOSITESA.2017.04.011

Nosrat Nezami, F., Gereke, T., Cherif, C., 2016. Analyses of interaction mechanisms during forming of multilayer carbon woven fabrics for composite applications. Compos. Part A Appl. Sci. Manuf. 84, 406–416. https://doi.org/10.1016/j.compositesa.2016.02.023

O'Brádaigh, C.M., Pipes, R.B., Mallon, P.J., 1991. Issues in diaphragm forming of continuous fiber reinforced thermoplastic composites. Polym. Compos. 12, 246–256. https://doi.org/10.1002/pc.750120406

Pazmino, J., Carvelli, V., Lomov, S. V., 2014. Micro-CT analysis of the internal deformed geometry of a non-crimp 3D orthogonal weave E-glass composite reinforcement. Compos. Part B Eng. 65, 147–157. https://doi.org/10.1016/j.compositesb.2013.11.024

Peirce, F.T., 1930. The "Handle" of Cloth As a Measurable Quantity. J. Text. Inst. Trans. 21, T377–T416. https://doi.org/10.1080/19447023008661529

Pickett, A.K., 2018. Introduction to Process and Mechanical Modelling of Engineering Composites, 465 p., ISBN 978-3-9819539-1-6

Plaut, R.H., 2020. Determining effective bending stiffness of fabrics and other materials from tests involving an added weight. Text. Res. J. 90, 101–109. https://doi.org/10.1177/0040517519858772

Plaut, R.H., 2015. Formulas to determine fabric bending rigidity from simple tests. Text. Res. J. 85, 884–894. https://doi.org/10.1177/0040517514553877

Potluri, P., Thammandra, V.S., 2007. Influence of uniaxial and biaxial tension on meso-scale geometry and strain fields in a woven composite. Compos. Struct. 77, 405–418. https://doi.org/10.1016/j.compstruct.2006.10.005

Rashidi, A., Milani, A.S., 2018. A multi-step biaxial bias extension test for wrinkling/de-wrinkling characterization of woven fabrics: Towards optimum forming design guidelines. Mater. Des. 146, 273–285. https://doi.org/10.1016/j.matdes.2018.02.075

Scerrato, D., Zhurba Eremeeva, I.A., Lekszycki, T., Rizzi, N.L., 2016. On the effect of shear stiffness on the plane deformation of linear second gradient pantographic sheets. ZAMM - J. Appl. Math. Mech. / Zeitschrift für Angew. Math. und Mech. 12, 1–12. https://doi.org/10.1002/zamm.201600066

Steigmann, D.J., Dell'Isola, F., 2015. Mechanical response of fabric sheets to three-dimensional bending, twisting, and stretching. Acta Mech. Sin. Xuebao 31, 373–382. https://doi.org/10.1007/s10409-015-0413-x

Turco, E., dell'Isola, F., Cazzani, A., Rizzi, N.L., 2016. Hencky-type discrete model for pantographic structures: numerical comparison with second gradient continuum models. Zeitschrift für Angew. Math. und Phys. 67, 85. https://doi.org/10.1007/s00033-016-0681-8

Turk, M.A., Vermes, B., Thompson, A.J., Belnoue, J.P.H., Hallett, S.R., Ivanov, D.S., 2020. Mitigating forming defects by local modification of dry preforms. Compos. Part A Appl. Sci. Manuf. 128. https://doi.org/10.1016/j.compositesa.2019.105643

Vanclooster, K., Lomov, S. V., Verpoest, I., 2009. Experimental validation of forming simulations of fabric reinforced polymers using an unsymmetrical mould configuration. Compos. Part A Appl. Sci. Manuf. 40, 530–539. https://doi.org/10.1016/j.compositesa.2009.02.005

Vernet, N., Ruiz, E., Advani, S., Alms, J.B., Aubert, M., Barburski, M., Barari, B., Beraud, J.M., Berg, D.C., Correia, N., Danzi, M., Delavière, T., Dickert, M., Di Fratta, C., Endruweit, A., Ermanni, P., Francucci, G., Garcia, J.A., George, A., Hahn, C., Klunker, F., Lomov, S. V., Long, A., Louis, B., Maldonado, J., Meier, R., Michaud, V., Perrin, H., Pillai, K., Rodriguez, E., Trochu, F., Verheyden, S., Weitgrefe, M., Xiong, W., Zaremba, S., Ziegmann, G., 2014. Experimental determination of the permeability of engineering textiles: Benchmark II. Compos. Part A Appl. Sci. Manuf. 61, 172–184. https://doi.org/10.1016/j.compositesa.2014.02.010

Wang, J., Wang, P., Hamila, N., Boisse, P., 2020. Mesoscopic analyses of the draping of 3D woven composite reinforcements based on macroscopic simulations. Compos. Struct. 112602. https://doi.org/10.1016/j.compstruct.2020.112602

Yu, F., Chen, S., Viisainen, J. V., Sutcliffe, M.P.F., Harper, L.T., Warrior, N.A., 2020. A macroscale finite element approach for simulating the bending behaviour of biaxial fabrics. Compos. Sci. Technol. 191. https://doi.org/10.1016/j.compscitech.2020.108078

Yu, W.. R., Pourboghrat, F., Chung, K., Zampaloni, M., Kang, T.. J., 2002. Non-orthogonal constitutive equation for woven fabric reinforced thermoplastic composites. Compos. Part A Appl. Sci. Manuf. 33, 1095–1105. https://doi.org/10.1016/S1359-835X(02)00053-2

Yu, W.R., Harrison, P., Long, A., 2005. Finite element forming simulation for non-crimp fabrics using a non-orthogonal constitutive equation. Compos. Part A Appl. Sci. Manuf. 36, 1079–1093. https://doi.org/10.1016/j.compositesa.2005.01.007

APPENDIX A (MECHANICAL PROPERTIES USED IN SIMULATIONS)

Mechanical properties used in the simulations reported in this paper are provided in this appendix.

A.1 TENSILE STIFFNESS

The tensile stiffness in the two tow directions was set at 3GPa, low enough to keep simulation times to manageable levels yet high enough to limit strains along the warp and weft tow directions to less than 1%; a level of strain typically measured in woven engineering fabrics due to un-crimping and compaction of the woven fabric when subject to tensile loads (Buet-Gautier and Boisse, 2001; Potluri and Thammandra, 2007).

A.2 SHEAR STIFFNESS

The shear stiffness of the fabrics was measured using a modified uniaxial bias extension test (with aluminium bonded to Region C of the specimen) both with and without anti-wrinkle plates (Harrison et al., 2018b). The latter allow more accurate measurement of the shear stiffness of the fabric at high shear angles (important if extreme deformations are to be simulated). Only data meeting the quality control criteria set out in (Alsayednoor et al., 2017) were used, i.e. an average specimen pre-shear angle of less than ~0.5^{o} and a standard deviation of the initial pre-shear angle less than ~2°. The data was normalised (Harrison et al., 2008, 2007; Harrison and Hartel, 2016) to produce the polynomial coefficients given in Table A1.

Table A1. *Polynomial coefficients of 9th order polynomial relating shear force per unit length to the shear angle.*

Polynomial Order, n	Shear Stiffness (N/m)	
	Glass	Carbon
0	0.0	0.0
1	0.159822729268449	0.008363859999423
2	0.197754695679862	0.029931112747270
3	-0.036483591558484	-0.005389213022195
4	0.002987530433924	0.000431377648224
5	-0.000133770268003	-0.000019096062688
6	0.000003435253055	0.000000504633357
7	-0.000000049744866	-0.000000007896077
8	0.000000000374354	0.000000000067115
9	-0.000000000001113	-0.000000000000235

A.3 OUT-OF-PLANE BENDING STIFFNESS

The out-of-plane bending stiffness per unit width was measured using a cantilever bending test with samples cut in the warp and weft directions using the procedure described in the test standard (ISO, 1998). Full details of the experiments and results can be found in (Harrison et al.,

2018a), values used in the simulations are: glass (warp direction) = 2.48 x10^{-3} Nm, glass (weft direction) = 7.71 x10^{-4} Nm, carbon (warp direction) = 2.3x10^{-4} Nm and carbon (weft direction) = 1.841x10^{-4} Nm. The ability of the modelling approach to accurately model the bending stiffness of the fabric when tested along the fibre directions was verified in (Harrison, 2016; Harrison et al., 2018a).

A.4 IN-PLANE BENDING STIFFNESS

The in-plane bending stiffness per unit width is estimated via inverse modelling of the in-plane kinematics of the modified uniaxial bias extension test. The process is described in detail in (Harrison et al., 2018a). The values determined by this method are around 2x that of the higher of the two out-of-plane bending stiffnesses. In-plan stiffness values used in the simulations are: glass (for both warp & weft directions) = 2.48x10^{-3} Nm, carbon (for both warp & weft directions) = 4.6 x10^{-4} Nm.

A.5 TORSIONAL STIFFNESS

Two techniques can be used to measure the torsional stiffness per unit width of the fabric. One method involves conducting a cantilever bending test the sample cut along the bias direction. Another method involves inverse modelling of the uniaxial bias extension test, adjusting the torsional stiffness to match the wrinkle onset angle in experiments and simulations. Values used in this investigation were derived using the latter method in Harrison et al., 2018c and are: glass (warp direction) = 2.33x10^{-3} Nm, glass (weft direction) = 1.56x10^{-3} Nm, carbon (warp direction) = 1.86x10^{-4} Nm carbon (weft direction) = 1.6x10^{-4} Nm.

Vitae

Dr Philip Harrison is a composite manufacturing and materials engineer with a BSc in Physics with Astrophysics from the University of Leeds and a PhD in Geophysics from the University of Aberystwyth. He is currently a Senior Lecturer at the University of Glasgow and has published over 100 research articles on materials and manufacturing. He previously worked with several polymer and polymer composites research groups including CEMEF in Sophia Antipolis, MATE in the Technical University of Eindhoven, the Composites Group at the University of Nottingham and INEGI in Porto.
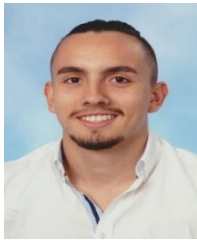
Mr Luis Gonzalez Camacho is a graduate with a first class BEng (Hons) degree in Mechanical Engineering awarded from the University of Glasgow in 2020.